



Universiteit
Leiden
The Netherlands

Molecules with ALMA at Planet-forming Scales (MAPS) XIII. HCO⁺ and disk ionization structure

Aikawa, Y.; Cataldi, G.; Yamato, Y.; Zhang, K.; Booth, A.S.; Furuya, K.; ... ; Wilner, D.J.





























Citation

Aikawa, Y., Cataldi, G., Yamato, Y., Zhang, K., Booth, A. S., Furuya, K., ... Wilner, D. J. (2021). Molecules with ALMA at Planet-forming Scales (MAPS): XIII. HCO⁺ and disk ionization structure. *The Astrophysical Journal Supplement Series*, 257(1).
doi:10.3847/1538-4365/ac143c

Version: Not Applicable (or Unknown)
License: [Leiden University Non-exclusive license](#)
Downloaded from: <https://hdl.handle.net/1887/3275430>

Note: To cite this publication please use the final published version (if applicable).

Molecules with ALMA at Planet-forming Scales (MAPS) XIII: HCO⁺ and disk ionization structure

YURI AIKAWA ¹, GIANNI CATALDI ^{1,2}, YOSHIHIDE YAMATO ¹, KE ZHANG ^{3,4,*}, ALICE S. BOOTH ^{5,6},
KENJI FURUYA ², SEAN M. ANDREWS ⁷, JAEHAN BAE ^{8,9,†}, EDWIN A. BERGIN ⁴, JENNIFER B. BERGNER ^{10,†},
ARTHUR D. BOSMAN ⁴, L. ILSEDORE CLEEVES ¹¹, IAN CZEKALA ^{12,13,14,15,16,†}, VIVIANA V. GUZMÁN ¹⁷,
JANE HUANG ^{4,7,†}, JOHN D. ILEE ⁶, CHARLES J. LAW ⁷, ROMANE LE GAL ^{7,18,19,20}, RYAN A. LOOMIS ²¹,
FRANÇOIS MÉNARD ¹⁹, HIDEKO NOMURA ², KARIN I. ÖBERG ⁷, CHUNHUA QI ⁷, KAMBER R. SCHWARZ ^{22,†},
RICHARD TEAGUE ⁷, TAKASHI TSUKAGOSHI ², CATHERINE WALSH ⁶ AND DAVID J. WILNER ⁷

¹*Department of Astronomy, Graduate School of Science, The University of Tokyo, 113-0033, Tokyo, Japan*

²*National Astronomical Observatory of Japan, 2-21-1 Osawa, Mitaka, Tokyo 181-8588, Japan*

³*Department of Astronomy, University of Wisconsin-Madison, 475 N Charter St, Madison, WI 53706*

⁴*Department of Astronomy, University of Michigan, 323 West Hall, 1085 S. University Avenue, Ann Arbor, MI 48109, USA*

⁵*Leiden Observatory, Leiden University, 2300 RA Leiden, the Netherlands*

⁶*School of Physics and Astronomy, University of Leeds, Leeds, LS2 9JT, UK*

⁷*Center for Astrophysics | Harvard & Smithsonian, 60 Garden St., Cambridge, MA 02138, USA*

⁸*Earth and Planets Laboratory, Carnegie Institution for Science, 5241 Broad Branch Road NW, Washington, DC 20015, USA*

⁹*Department of Astronomy, University of Florida, Gainesville, FL 32611, USA*

¹⁰*University of Chicago Department of the Geophysical Sciences, Chicago, IL 60637, USA*

¹¹*Department of Astronomy, University of Virginia, Charlottesville, VA 22904, USA*

¹²*Department of Astronomy and Astrophysics, 525 Davey Laboratory, The Pennsylvania State University, University Park, PA 16802, USA*

¹³*Center for Exoplanets and Habitable Worlds, 525 Davey Laboratory, The Pennsylvania State University, University Park, PA 16802, USA*

¹⁴*Center for Astrostatistics, 525 Davey Laboratory, The Pennsylvania State University, University Park, PA 16802, USA*

¹⁵*Institute for Computational & Data Sciences, The Pennsylvania State University, University Park, PA 16802, USA*

¹⁶*Department of Astronomy, 501 Campbell Hall, University of California, Berkeley, CA 94720-3411, USA*

¹⁷*Instituto de Astrofísica, Pontificia Universidad Católica de Chile, Av. Vicuña Mackenna 4860, 7820436 Macul, Santiago, Chile*

¹⁸*IRAP, Université de Toulouse, CNRS, CNES, UT3, 31400 Toulouse, France*

¹⁹*Univ. Grenoble Alpes, CNRS, IPAG, F-38000 Grenoble, France*

²⁰*IRAM, 300 rue de la piscine, F-38406 Saint-Martin d'Hères, France*

²¹*National Radio Astronomy Observatory, 520 Edgemont Rd., Charlottesville, VA 22903, USA*

²²*Lunar and Planetary Laboratory, University of Arizona, 1629 E. University Blvd, Tucson, AZ 85721, USA*

(Received March 3, 2021; Revised June 16, 2021; Accepted June 17, 2021)

Submitted to ApJ

ABSTRACT

We observed HCO⁺ $J = 1 - 0$ and H¹³CO⁺ $J = 1 - 0$ emission towards the five protoplanetary disks around IM Lup, GM Aur, AS 209, HD 163296, and MWC 480 as part of the MAPS project. HCO⁺ is detected and mapped at 0.3'' resolution in all five disks, while H¹³CO⁺ is detected (SNR > 6 σ) towards GM Aur and HD 163296 and tentatively detected (SNR > 3 σ) towards the other disks by a matched filter analysis. Inside a radius of $R \sim 100$ au, the HCO⁺ column density is flat or shows a central dip. At outer radii ($\gtrsim 100$ au), the HCO⁺ column density decreases outwards, while the column density ratio of HCO⁺/CO is mostly in the range of $\sim 10^{-5} - 10^{-4}$. We derived the HCO⁺ abundance in the warm CO-rich layer, where HCO⁺ is expected to be the dominant molecular ion. At $R \gtrsim 100$ au, the HCO⁺ abundance is $\sim 3 \times 10^{-11} - 3 \times 10^{-10}$, which is consistent with a template disk model with X-ray ionization. At the smaller radii, the abundance decreases inwards, which indicates that the

ionization degree is lower in denser gas, especially inside the CO snow line, where the CO-rich layer is in the midplane. Comparison of template disk models with the column densities of HCO^+ , N_2H^+ , and N_2D^+ indicates that the midplane ionization rate is $\gtrsim 10^{-18} \text{ s}^{-1}$ for the disks around IM Lup, AS 209, and HD 163296. We also find hints of an increased HCO^+ abundance around the location of dust continuum gaps in AS 209, HD 163296, and MWC 480. **This paper is part of the MAPS special issue of the Astrophysical Journal Supplement.**

Keywords: Astrochemistry — Exoplanet formation — Interferometry — Millimeter astronomy — Protoplanetary disks

1. INTRODUCTION

Protoplanetary disks are the birth site of planetary systems including our Solar System. The rate and degree of ionization are important parameters for both the physical and chemical evolution of the disk, and thus for the formation of planetary systems. The disk gas is much denser, and thus its ionization degree x_i , which is the relative abundance of electrons to H_2 , is much lower than in parental molecular clouds (e.g. Umebayashi & Nakano 1988)¹. Yet the ionization degree is expected to be sufficient for the gas to be partially coupled with the magnetic fields present in the disk, which could induce magneto-hydrodynamic instabilities, disk winds, and thus the angular momentum transfer needed for mass accretion (e.g. Suzuki & Inutsuka 2009; Bai & Stone 2013). More specifically, the ionization degree, and thus the coupling between gas and magnetic fields (i.e. non-ideal MHD effects) should vary spatially within the disk, which affects the physical structure of the disk (e.g. Béthune et al. 2017). Ionization also triggers ion-molecule reactions in the disk. For example, carbon monoxide, which is the main tracer of disk gas, can be converted to other species by ion-molecule reactions within the typical evolutionary timescale of the disk (10^6 yr), if the ionization rate ζ is similar to or higher than the cosmic-ray ionization rate in the ISM (10^{-17} s^{-1} ; Furuya & Aikawa 2014; Bergin et al. 2014; Bosman et al. 2018; Schwarz et al. 2018).

The ionization degree is determined by the ionization rate, gas density, and number density and size distribution of dust grains. For protoplanetary disks, there are several possible ionization sources: X-rays from the central star, cosmic rays (CRs) and stellar energetic particles, and the decay of short-lived radio active nuclei (SLR) (e.g. Umebayashi & Nakano 1981; Glassgold et al. 1997; Umebayashi & Nakano 2009; Rab et al. 2017). X-rays are the dominant ionization source in the disk surface. However, X-rays are significantly attenuated before reaching the disk midplane. The attenuation length corresponds to a hydrogen column density of $N_{\text{H}} \sim 10^{22} \text{ cm}^{-2}$ at 1 keV, while the hydrogen column densities of our target disks are $\sim 10^{23} - 10^{25} \text{ cm}^{-2}$ at the radius of 100 au (Zhang & MAPS team 2021). Although the attenuation length is larger at higher energies, the X-ray ionization rate is still expected to be $\lesssim 10^{-18} \text{ s}^{-1}$ in the midplane (e.g. §4) (see also Rab et al. 2018). The cosmic-ray ionization rate is $\sim 5 \times 10^{-17} \text{ s}^{-1}$ in molecular clouds (Dalgarno 2006), and its attenuation length is much larger than that of X-rays. While Umebayashi & Nakano (1981) evaluated the attenuation length to be 96 g cm^{-2} , more recent work by Padovani et al. (2018) reassessed the propagation of CR particles and obtained an even larger attenuation length. But CRs can be scattered by magnetized stellar winds and/or magnetic fields in the disk (e.g. Umebayashi & Nakano 1981; Cleeves et al. 2014; Padovani et al. 2018). Stellar energetic particles could also be disturbed by magnetic fields. Finally, the ionization rate from the decay of ^{26}Al is estimated to be 10^{-18} s^{-1} in the primordial Solar System based on meteorite analysis (e.g. Umebayashi & Nakano 2009). While the abundance of SLRs should vary among star-forming regions, recent chemo-hydrodynamic simulations of the Milky Way Galaxy predict that the abundance of ^{26}Al in the primordial Solar System may be typical for other star-forming regions (Fujimoto et al. 2018). In summary, the dominant ionization source and ionization degree should vary spatially within the disk and could be different between disks.

The importance of understanding ionization processes motivates the observation of molecular ions in protoplanetary disks. Theoretical models show that the major molecular ions in disks are H_3^+ , HCO^+ , N_2H^+ , and their deuterated isotopologues (e.g. Aikawa & Herbst 2001; Bergin et al. 2007; Willacy 2007; Aikawa et al. 2015, 2018). The most abundant molecular ion varies both radially and vertically in disks (Figure 1). The disk surface is the Photon Dominated Region (PDR); photoionization makes atomic ions such as C^+ and S^+ the main charge carriers. Deeper in the disk,

* NASA Hubble Fellow

† NASA Hubble Fellowship Program Sagan Fellow

¹ Considering neutrality, the electron abundance should be the same as the total abundance of cations. In dense midplane regions, grain particles can be the dominant charge carrier.

H_3^+ becomes the most abundant ion, while HCO^+ becomes dominant when the abundance ratio $n(\text{CO})/n(\text{e})$ is higher than $\sim 10^3$, where $n(i)$ denotes the number density of species i (Aikawa et al. 2015). In the regions where $T < 20$ K (i.e. below the CO snow surface and outside the CO snow line), CO freezes out onto grains, which enhances the N_2H^+ abundance. As temperature declines towards deeper layers, the dominant ion changes from N_2H^+ to H_3^+ and its deuterated isotopologues. Unfortunately, H_3^+ cannot be observed at millimeter wavelengths, and its deuterated isotopologues have not been detected in disks so far. N_2D^+ is considered to be an alternative probe to constrain the ionization degree in the cold midplane (Cleeves et al. 2014).

While the rotational transitions of HCO^+ , N_2H^+ , and their isotopologues have been observed towards several disks, a quantitative evaluation of their column densities and the disk ionization degree has been reported only in a limited number of references. Öberg et al. (2011a) used the IRAM 30 m telescope to observe $\text{H}^{13}\text{CO}^+ J = 3 - 2$ in the disk of DM Tau. They combined their observation with previous Submillimeter Array (SMA) data of $\text{N}_2\text{H}^+ J = 3 - 2$, $\text{HCO}^+ J = 3 - 2$, and $\text{DCO}^+ J = 3 - 2$ to estimate the ionization degree in three temperature regions of the disk: in the upper warm molecular layer ($T > 20$ K), the ionization degree x_i is estimated to be 4×10^{-10} based on the HCO^+ data. In the cooler molecular layer ($T = 16 - 20$ K), where N_2H^+ and DCO^+ would be abundant, x_i is derived to be 3×10^{-11} , while in the cold, dense midplane ($T < 16$ K), the non-detection of H_2D^+ constrains x_i to be $< 3 \times 10^{-10}$. Teague et al. (2015) observed $\text{HCO}^+ J = 1 - 0$ and $J = 3 - 2$, and $\text{DCO}^+ J = 3 - 2$ in DM Tau at $\sim 1.5''$ resolution using the Plateau de Bure Interferometer (PdBI). The column densities of HCO^+ and DCO^+ at a radius of 100 au are derived to be 9.8×10^{12} and $1.2 \times 10^{12} \text{ cm}^{-2}$, respectively. They derive an ionization degree of $\sim 10^{-7}$ from the abundance ratio of $\text{DCO}^+/\text{HCO}^+$, assuming steady state balance between $\text{H}_3^+ + \text{HD} \rightarrow \text{H}_2\text{D}^+ + \text{H}_2$, $\text{H}_2\text{D}^+ + \text{CO} \rightarrow \text{DCO}^+ + \text{H}_2$, and the destruction of DCO^+ (Caselli et al. 2002). Cleeves et al. (2015) calculated chemical models of the disk around TW Hya for various cosmic-ray ionization rates ζ_{CR} and X-ray spectra. Instead of evaluating molecular column densities from the observational data, they calculated the disk-integrated flux of molecular lines from the models to compare with their own HCO^+ and $\text{H}^{13}\text{CO}^+ J = 3 - 2$ observations of TW Hya, and HCO^+ , H^{13}CO^+ , and N_2H^+ data from the literature (e.g. Qi et al. 2013a,b). They concluded that the observations are best reproduced by the model with low CR ionization rate $\zeta_{\text{CR}} \lesssim 10^{-19} \text{ s}^{-1}$ and modest X-ray spectra, in which the ionization degree is $\sim 10^{-11} - 10^{-10}$ near the midplane outside of a radius of ~ 100 au. Since the ionization degree varies spatially and between disks, observations with higher spatial resolution and towards more targets are highly desirable.

In light of the ring-gap structures observed in the millimeter dust continuum of many disks in recent years (e.g. Andrews et al. 2018; Huang et al. 2018; Cieza et al. 2021), it is also interesting to investigate whether and how the molecular ion abundances and ionization degree correlate with the dust substructures. Theoretical studies predict that HCO^+ is sensitive to, and thus could be a good probe of, gas density and/or small dust abundance. In the region where HCO^+ is the most abundant positive charge carrier, its abundance (i.e. ionization degree) should be proportional to $n_{\text{H}}^{-1/2}$ (e.g. Duley & Williams 1984). In the gap region, the ionization degree could also be enhanced due to deeper penetration of X-rays. Aikawa & Nomura (2006), on the other hand, showed that the HCO^+ column density declines as the abundance of sub-micron sized dust grains decreases with grain growth. This is because the PDR, in which atomic ions dominate over molecular ions, extends deeper into the disk when the abundance of sub-micron dust grains decreases. Similar results are obtained in models of disks around Herbig Ae stars (Jonkheid et al. 2007) (see also Wakelam et al. 2019). While these models do not include any ring-gap structures, they indicate that the HCO^+ abundance could vary over the substructures. The HCO^+ abundance would be higher in the gap than in the ring, if the gas density is lower but the UV attenuation is sufficient in the gap. On the other hand, the HCO^+ abundance would be lower in the gap if the UV penetration is significant (see also Smirnov-Pinchukov et al. 2020).

In the present work, we analyze the $J = 1 - 0$ transition of HCO^+ and H^{13}CO^+ towards five disks around IM Lup, GM Aur, AS 209, HD 163296, and MWC 480 observed as a part of the Molecules with ALMA at Planet-forming Scales (MAPS) Large Program (Öberg & MAPS team 2021, project code 2018.1.01055.L). For a given column density of HCO^+ at a lukewarm temperature (a few tens of K), which corresponds to the CO rich molecular layer in the disk, the $J = 1 - 0$ line tends to be optically thinner than higher transitions, and thus useful to derive the column density. Our spatial resolution, $0.3''$, is high enough to investigate the radial distribution of HCO^+ and to marginally resolve the continuum gap regions. We also combine our results with the analysis of CO isotopologues, N_2H^+ , and N_2D^+ in the companion MAPS papers by Zhang & MAPS team (2021) and Cataldi & MAPS team (2021) to estimate the radial variation in the ionization degree and the ionization rate in the disks. Various data products of the MAPS project, including the present work, such as reduced observational data, zeroth-moment maps, as well as derived HCO^+ column densities can be downloaded at www.alma-maps.info.

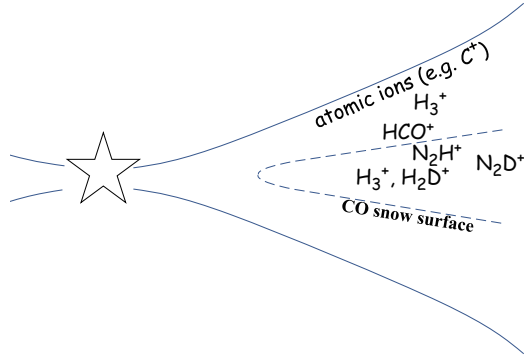


Figure 1. Schematic distribution of major ions in protoplanetary disks.

Table 1. Molecular data of the targeted lines taken from the CDMS database.

transition	frequency [GHz]	A_{ij} ^a [s ⁻¹]	E_u ^b [K]
HCO ⁺ J = 1–0	89.1885247	4.2512×10^{-5}	4.28
H ¹³ CO ⁺ J = 1–0	86.7542884	3.8534×10^{-5}	4.16

^aEinstein A coefficient.

^bUpper state energy.

The outline of this paper is as follows. We briefly describe the observations in §2. §3 describes the observational results: the zeroth moment maps, radial emission profiles, azimuthally averaged spectra, and molecular column densities. We derive the HCO⁺ abundance, which corresponds to a lower limit of the ionization degree in the warm molecular layer, and compare our results with a template disk chemistry model in §4. Our conclusions are presented in §5.

2. OBSERVATIONS

The observational setup chosen by MAPS covered four spectral setups: two in Band 3 at ~ 3 mm and two in Band 6 at ~ 1 mm. The $J = 1 - 0$ transitions of HCO⁺ and H¹³CO⁺ are in one of the Band 3 setups. The spectral resolution is 0.237 km s^{-1} for HCO⁺ and 0.488 km s^{-1} for H¹³CO⁺. Molecular data for the targeted lines is taken from the CDMS database² (Müller et al. 2001; Endres et al. 2016) and summarized in table 1.

Two array configurations were used: a short baseline configuration that was sensitive to extended structure, and a long baseline configuration to achieve high angular resolution. The details of the data calibration are described in Öberg & MAPS team (2021). The MAPS collaboration produced images from the calibrated visibilities using the CLEAN algorithm implemented in the CASA `tclean` task. Details of the imaging procedure are described in Czekala & MAPS team (2021). We use the fiducial images provided by MAPS, which have a $0''.3$ circular beam. This beam size corresponds to a physical size of 30.3 au at the distance of HD 163296, which is the closest target, and 48.6 au at the distance of MWC 480, which is the most distant. Basic properties of the data cubes such as noise levels are summarized in Table 11 and 12 in Öberg & MAPS team (2021).

3. OBSERVATIONAL RESULTS

3.1. Zeroth moment maps, disk-integrated fluxes, and radial emission profiles

The MAPS collaboration produced zeroth moment maps by applying a Keplerian mask to the data cubes and integrating over the velocity axis (Law & MAPS team 2021a). The mask parameters are conservatively chosen to incorporate all ¹³CO $J = 2 - 1$ emission, which is the most widespread emission of any species except for CO $J = 2 - 1$. The mask parameters for the five disks are summarized in Table 1 in Czekala & MAPS team (2021). The stellar masses

² <https://cdms.astro.uni-koeln.de/>

adopted for the generation of the masks are listed in Table 1 in [Öberg & MAPS team \(2021\)](#). These maps were used for all scientific analysis, in particular to derive radial emission profiles ([Law & MAPS team 2021a](#)). A Keplerian mask, however, introduces spatial variance in noise distribution, since the number of channels summed to create the zeroth moment maps vary spatially. The discontinuous noise distribution occasionally causes arc-like artefacts, which could be mistaken as real substructure, in the central regions. To mitigate such artefacts, MAPS also produced “hybrid” zeroth moment maps by combining a Keplerian mask and a smoothed σ -clip mask (thus their name “hybrid”, see [Law & MAPS team 2021a](#), Appendix A). The latter removes the pixels with a S/N below a given threshold. We emphasize that by using a clipping mask with a threshold larger than 0σ , some emission is inevitably lost. Therefore, the hybrid zeroth moment maps are for presentational purposes only, and are not used for any quantitative analysis.

In Figure 2, we show hybrid zeroth moment maps for $\text{HCO}^+ J = 1 - 0$ and $\text{H}^{13}\text{CO}^+ J = 1 - 0$. We choose the best-looking σ -clip value by visual inspection: 1σ for $\text{HCO}^+ J = 1 - 0$ towards IM Lup, and 0σ for the other maps. Hybrid zeroth moment maps with a $0''.5$ tapered beam are shown in Figure 13 in Appendix A; the faint emission is more easily seen in the lower spatial resolution images.

The $\text{HCO}^+ J = 1 - 0$ line is clearly detected in all five disks. The emission is relatively bright inside a radius of ~ 200 au, while its diffuse emission extends to $\gtrsim 400$ au, except for the disk of AS 209, in which the emission extends only up to $R \sim 300$ au. In AS 209, the emission from the west side of the disk is absorbed by a foreground cloud, which happens to have a similar line-of-sight velocity ([Öberg et al. 2011b](#)). We thus performed all analysis for AS 209 only on the un-obscured east side of the disk within a ± 55 degree wedge centered on the semi-major axis ([Teague et al. 2018b](#); [Law & MAPS team 2021a](#)). The emission of $\text{H}^{13}\text{CO}^+ J = 1 - 0$ is very weak and is not clearly seen in the zeroth moment maps.

Disk-integrated fluxes of $\text{HCO}^+ J = 1 - 0$ and $\text{H}^{13}\text{CO}^+ J = 1 - 0$ are presented in Table 2. These were calculated by integrating the flux within a Keplerian mask. The radial extent of the Keplerian mask is different from that used for the zeroth moment maps. For HCO^+ , the radial extent of the mask is visually determined from the extent of the emission seen in the radial emission profile (see Figure 3 and Table 2). For H^{13}CO^+ , we measured fluxes by using the same radial extents as for HCO^+ . In an attempt to increase the SNR, we computed additional fluxes by adopting the same radial extent as the Keplerian models that maximize the SNR in the matched filter analysis in the uv plane (Appendix B, Figure 14), as shown in the right column of Table 2. Errors were calculated by repeating the flux measurement procedure at off-source positions and taking the standard deviation of the off-source fluxes. A 10% flux calibration error was added in quadrature. If the resulting SNR was smaller than 3, Table 2 reports the 3σ upper limit. To calculate these disk-integrated fluxes and errors, we used the image cubes that are not corrected for the primary beam. This is because for primary beam corrected images, the noise increases towards the edges of the image, making our approach to estimate the error from off-source positions invalid. However, we verified that the difference to fluxes extracted from primary beam corrected images is negligible. For deriving radially resolved column density profiles, we use the primary beam corrected images.

H^{13}CO^+ is seen with $\text{SNR} > 3$ for IM Lup, GM Aur, and HD 163296, if we use the masks with the extent informed by the matched filter analysis. The matched filter analysis itself (Appendix B) gives a response larger than 6σ for GM Aur and HD 163296, and larger than 3σ for the other disks. Thus, we consider $\text{H}^{13}\text{CO}^+ J = 1 - 0$ detected in GM Aur and HD 163296, and tentatively detected for the other three disks. We note that the values in Table 2 are different from those in Table 12 in [Öberg & MAPS team \(2021\)](#), who adopted the same Keplerian masks to generate zeroth moment maps and to estimate disk-integrated fluxes.

Figure 3 shows the radial emission profiles of the $J = 1 - 0$ transitions of HCO^+ and H^{13}CO^+ . These profiles are produced by azimuthal averaging the zeroth moment maps that were produced with a Keplerian mask only (i.e. without a σ -clip mask). The inclination and position angles of each disk are listed in Table 1 in [Öberg & MAPS team \(2021\)](#). Since HCO^+ is expected to be formed by $\text{CO} + \text{H}_3^+$ and to be a dominant molecular ion in CO gas rich layers, we also plotted the radial emission profile of $\text{C}^{18}\text{O} J = 1 - 0$ derived by [Law & MAPS team \(2021a\)](#). The vertical lines indicate the radius of rings (solid), gaps (dashed), and the dust disk edge (dotted) observed in the millimeter dust continuum ([Huang et al. 2018](#); [Long et al. 2018](#); [Liu et al. 2019](#); [Sierra & MAPS team 2021](#); [Law & MAPS team 2021a](#)). Both HCO^+ and C^{18}O emission extend out to several 100 au. In the IM Lup disk, the radial emission profile of $\text{HCO}^+ J = 1 - 0$ is similar to that of C^{18}O , showing a ring-like distribution, although the peak position of the HCO^+ emission is ~ 36 au outside of the C^{18}O peak. In GM Aur, on the other hand, both the C^{18}O and HCO^+ emission are centrally peaked. The radial emission profiles of C^{18}O and HCO^+ are quite different in AS 209: around a radius of ~ 77 au, the HCO^+ emission has a local maximum, while the radial gradient of C^{18}O changes from negative

Table 2. Disk-integrated fluxes. Upper limits are at 3σ significance.

	HCO ⁺ 1–0			H ¹³ CO ⁺ 1–0 ^a			H ¹³ CO ⁺ 1–0 ^b		
	r_{\min}^c	r_{\max}^d	flux	r_{\min}	r_{\max}	flux	r_{\min}	r_{\max}	flux
	[au]	[au]	[mJy km s ⁻¹]	[au]	[au]	[mJy km s ⁻¹]	[au]	[au]	[mJy km s ⁻¹]
IM Lup	0	700	519 ± 53	0	700	< 46	0	400	23 ± 6
GM Aur	0	500	412 ± 42	0	500	< 43	0	400	27 ± 7
AS 209	0	300	178 ± 19	0	300	< 33	0	200	< 26
HD 163296	0	550	1002 ± 101	0	550	< 54	50	400	27 ± 7
MWC 480	0	550	323 ± 34	0	550	< 34	50	100	< 18

^aFor a Keplerian mask with the same radial extent as used for HCO⁺ 1–0.

^bFor a Keplerian mask with the same radial extent as the matched filter that maximises the SNR of the filter response (see Appendix B and Fig. 14).

^cMinimum radius of the Keplerian mask.

^dMaximum radius of the Keplerian mask.

to plateau. Interestingly, the peak position of the HCO⁺ emission coincides with that of a dust continuum ring. In the disks around the Herbig Ae stars, HD 163296 and MWC 480, the HCO⁺ emission shows a central dip, while C¹⁸O is flat for HD 163296 and centrally peaked for MWC 480.

The intensity ratio of the C¹⁸O and HCO⁺ lines varies significantly with radius and among objects. For example, the ratio reaches ~ 5 towards the center of the MWC 480 disk, while HCO⁺ is brighter than C¹⁸O around $R \sim 77$ au in AS 209. Although this indicates that the abundance (column density) ratio of HCO⁺ to C¹⁸O also varies, we need to consider the line optical depth. Under LTE conditions with an excitation temperature of 30 K, which is a typical temperature in the warm molecular layers, the optical depth of C¹⁸O $J = 1 - 0$ reaches unity for a C¹⁶O column density of $\sim 6 \times 10^{18}$ cm⁻², assuming a ¹⁶O/¹⁸O isotope ratio of 557 (Wilson 1999). Zhang & MAPS team (2021) derived the radial column density distribution of CO by analyzing several transitions of CO and its isotopologues. The CO column density exceeds 6×10^{18} cm⁻² inside a radius of ~ 100 au in the GM Aur, HD 163296, and MWC 480 disks. At least for these inner radii, C¹⁸O $J = 1 - 0$ is optically thick, and thus the intensity ratio of C¹⁸O to HCO⁺ does not reflect their column density ratio. We also need to evaluate the optical depth of HCO⁺ to derive its column density; the optical depth of HCO⁺ $J = 1 - 0$ reaches unity for a HCO⁺ column density of $\sim 1 \times 10^{13}$ cm⁻² under LTE conditions at a temperature of 30 K.

3.2. Azimuthally averaged spectra and radial profiles of the HCO⁺ column density

In order to evaluate the radial profile of the optical depth and column density of HCO⁺, we first derive the azimuthally averaged spectrum for radial bins with a width of half the beam size. Due to the Keplerian rotation of the disk, at each spatial location in the data cube, the spectrum is shifted with respect to the systemic velocity. We thus shift each spectrum by the Keplerian velocity projected to the line of sight before averaging the spectra azimuthally. This results in all individual spectra being centered at the systemic velocity, which increases the S/N ratio of the azimuthally averaged spectrum (Yen et al. 2016; Teague et al. 2016; Matrà et al. 2017). The calculation of the error bars of the averaged spectrum is described in detail in Appendix D of Cataldi & MAPS team (2021). Briefly, we calculate both the standard deviation of the spectrum in regions without line emission, and an analytical error bar based on the number of independent samples included in the average. We then adopt the maximum of the two as our final error bar. Figure 4 shows examples of extracted spectra of HD 163296. The full gallery of spectra is found in Appendix C.

We then calculate the column density of HCO⁺, $N(\text{HCO}^+)$, at each radial bin by simultaneously fitting the azimuthally averaged spectra of HCO⁺ and H¹³CO⁺. We employ the same fitting procedure as Cataldi & MAPS team (2021). Briefly, for a given HCO⁺ column density, we compute HCO⁺ $J = 1 - 0$ and H¹³CO⁺ $J = 1 - 0$ model spectra that can be compared to the data. There are five free parameters: the logarithm of the HCO⁺ column density, the excitation temperature, an offset Δv of the line center with respect to the systemic velocity for each line, and the full width at half maximum (FWHM) of the Gaussian kernel with which the model spectra are convolved to mimic observational broadening. The H¹³CO⁺ column density is fixed to 1/68 of the HCO⁺ column density (Milam et al. 2005). We use an MCMC method implemented in the emcee package (Foreman-Mackey et al. 2013) to explore the

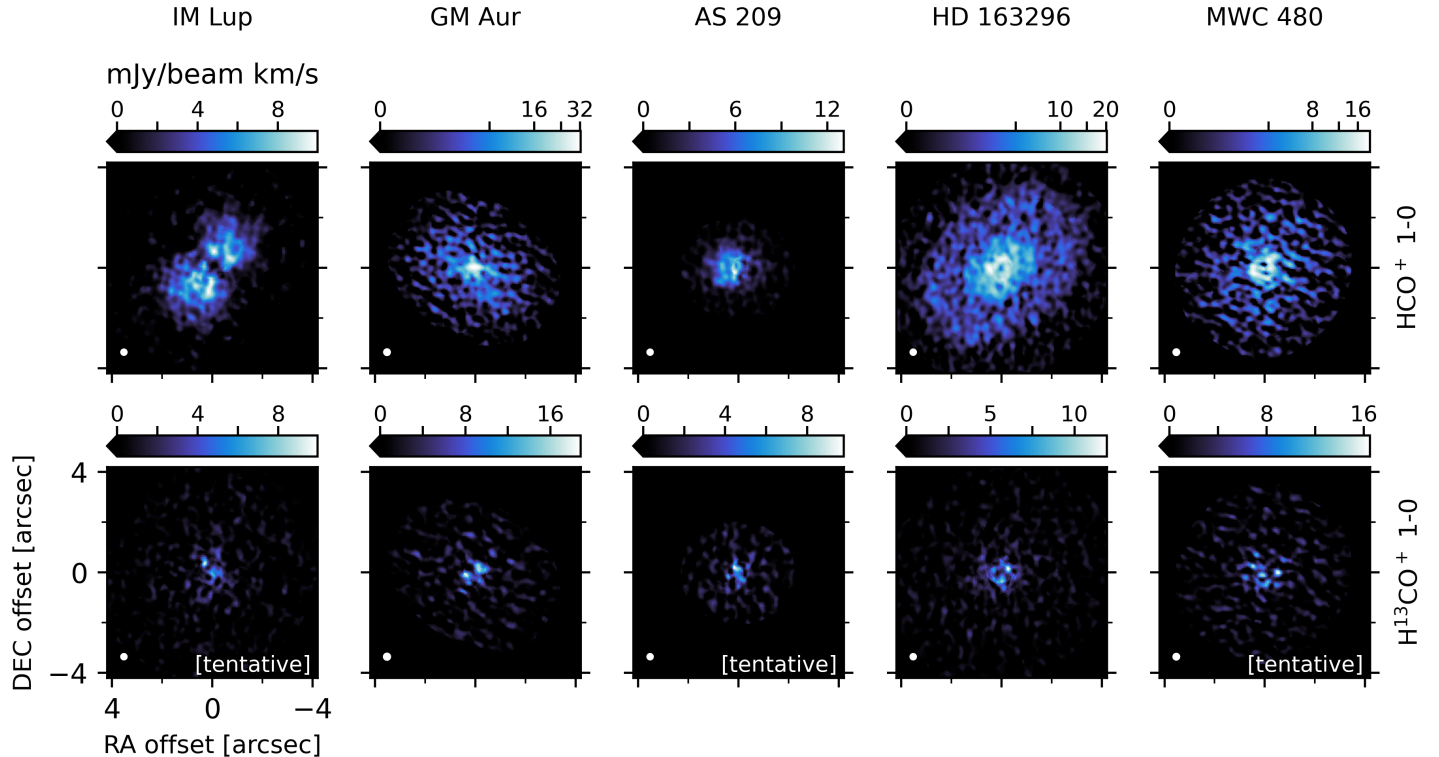


Figure 2. Gallery of hybrid zeroth moment maps for $\text{HCO}^+ J = 1 - 0$ (top row) and $\text{H}^{13}\text{CO}^+ J = 1 - 0$ (bottom row) for the MAPS sample, ordered from left to right by increasing stellar mass (see Öberg & MAPS team 2021, table 1). These maps were generated by combining a Keplerian mask with a smoothed σ -clip mask (Appendix A of Law & MAPS team 2021a). The color scales employ either linear or arcsinh stretches, with the lower end saturating at $0 \text{ mJy beam}^{-1} \text{ km s}^{-1}$. The synthesized beam is shown by the white ellipse in the lower left of each panel. Due to the use of a mask, the noise level is not constant across a map. Lines that are only tentatively detected in total flux or matched filter are marked in the lower right of the panel.

parameter space and assume flat priors. We employ 200 walkers taking 5000 steps each, and discard the first 2500 steps from the analysis. The free parameters and the prior boundaries are listed in Table 3. The full details of the fitting procedure can be found in Cataldi & MAPS team (2021). Figure 4 shows examples of model spectra fitted to the HD 163296 data. The full gallery of models is shown in Appendix C.

Figure 5 and 6 show the optical depths and excitation temperature derived by fitting the azimuthally averaged spectra. We find that $\text{HCO}^+ J = 1 - 0$ is optically thick at the column density peaks. However, we are still able to constrain the HCO^+ column density because the $\text{H}^{13}\text{CO}^+ J = 1 - 0$ transition is in the optically thin regime. The top panels in Figure 7 present the derived HCO^+ column densities.

The excitation temperature is poorly constrained for large radial regions of the disks, as shown in Fig. 6. However, at least a lower limit on the excitation temperature can be placed in some disk locations. The innermost $\sim 50 \text{ au}$ of GM Aur stand out with an apparently well constrained $T_{\text{ex}} \approx 90 \text{ K}$. This region also requires a large FWHM of 17 km s^{-1} . These rather extreme parameters might indicate that the fit is not reliable. In fact, considerable broadening is seen for all disks for the two innermost radial bins (i.e. within one beam FWHM from the disk center) due to beam smearing of the large velocity gradient in the inner disk (see Figures 16a). Therefore, the column density estimates for the two innermost radial bins should be considered with caution.

In Appendix D, we show optical depth and column density profiles for additional fits where the excitation temperature has been fixed to 30 K , which is a typical temperature for the warm molecular layer where HCO^+ is expected to be present. The corresponding models are shown in Figure 16a. The column densities generally agree well with the fits where T_{ex} is a free parameter, as can be seen in Fig. 17. Furthermore, for both fits, the model spectra fit the data well (Figure 16a). One exception is the region inwards of $\sim 150 \text{ au}$ towards GM Aur where the models with T_{ex} as a free parameter generally provide a better fit, especially for the two innermost radial bins discussed in the previous

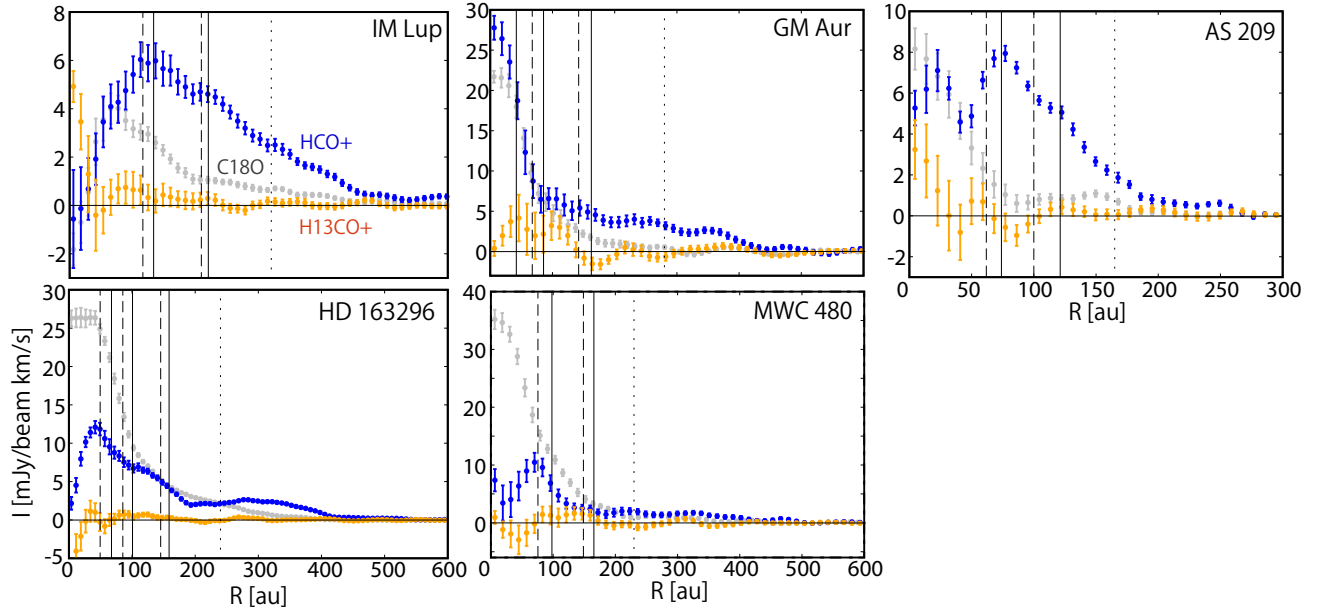


Figure 3. Radial emission profiles of $\text{HCO}^+ J = 1 - 0$, $\text{H}^{13}\text{CO}^+ J = 1 - 0$, and $\text{C}^{18}\text{O} J = 1 - 0$ for IM Lup, GM Aur, AS 209, HD 163296, and MWC 480. The error bar shows the $\pm 1\sigma$ error. The size of the radial bins is $0.075''$, which is a quarter of the beam size. The vertical lines indicate the positions of rings (solid), gaps (dashed), and the edge of millimeter dust continuum (dotted) referring to Huang et al. (2018); Long et al. (2018); Liu et al. (2019); Law & MAPS team (2021a) (see also Sierra & MAPS team 2021).

Table 3. Free parameters for fitting of azimuthally averaged spectra to derive the HCO^+ column density.

Parameter	prior low ^a	prior high ^b	unit
$\log N_{\text{HCO}^+}$	1	16	$\log([\text{cm}^{-2}])$
T_{ex}	10	100	[K]
$\text{FWHM}_{\text{kernel}}$	0.5 ^c	variable ^d	$[\text{km s}^{-1}]$
Δv_{HCO^+} ^e	-0.3	0.3	$[\text{km s}^{-1}]$
$\Delta v_{\text{H}^{13}\text{CO}^+}$	-0.3	0.3	$[\text{km s}^{-1}]$

^aLower bound of flat prior.

^bUpper bound of flat prior.

^cEqual to the channel width.

^dInitial value for innermost radial bin is 20 km s^{-1} . Dynamically adjusted when sequentially fitting larger and larger radii (see Cataldi & MAPS team 2021, for details).

^eOffset of the line center with respect to the systemic velocity.

paragraph (Fig. 16a). The other exception is the region inwards of 76 au towards HD 163296, where the fits with $T_{\text{ex}} = 30 \text{ K}$ underpredict the HCO^+ emission and overpredict the H^{13}CO^+ emission (Fig. 16a). Here, the models with T_{ex} as a free parameter provide a better fit and predict a column density smaller by a factor of a few compared to the fits where $T_{\text{ex}} = 30 \text{ K}$.

In Figure 7, we also plot the column densities of CO which are derived from $\text{C}^{18}\text{O} J = 2 - 1$ emission in Zhang & MAPS team (2021). For each disk, they constructed a thermo-chemical model which reproduces the SED. The model provides the 2D (R, Z) distributions of temperature and CO abundance. Then they introduced a CO depletion factor, which is varied from 0.001 to 50 with a step-size of 1.1 in a logarithmic scale, at each radial bin, and calculated the CO flux for grid of models to find the best fit depletion factor. The uncertainty in the CO column density is thus 10 %

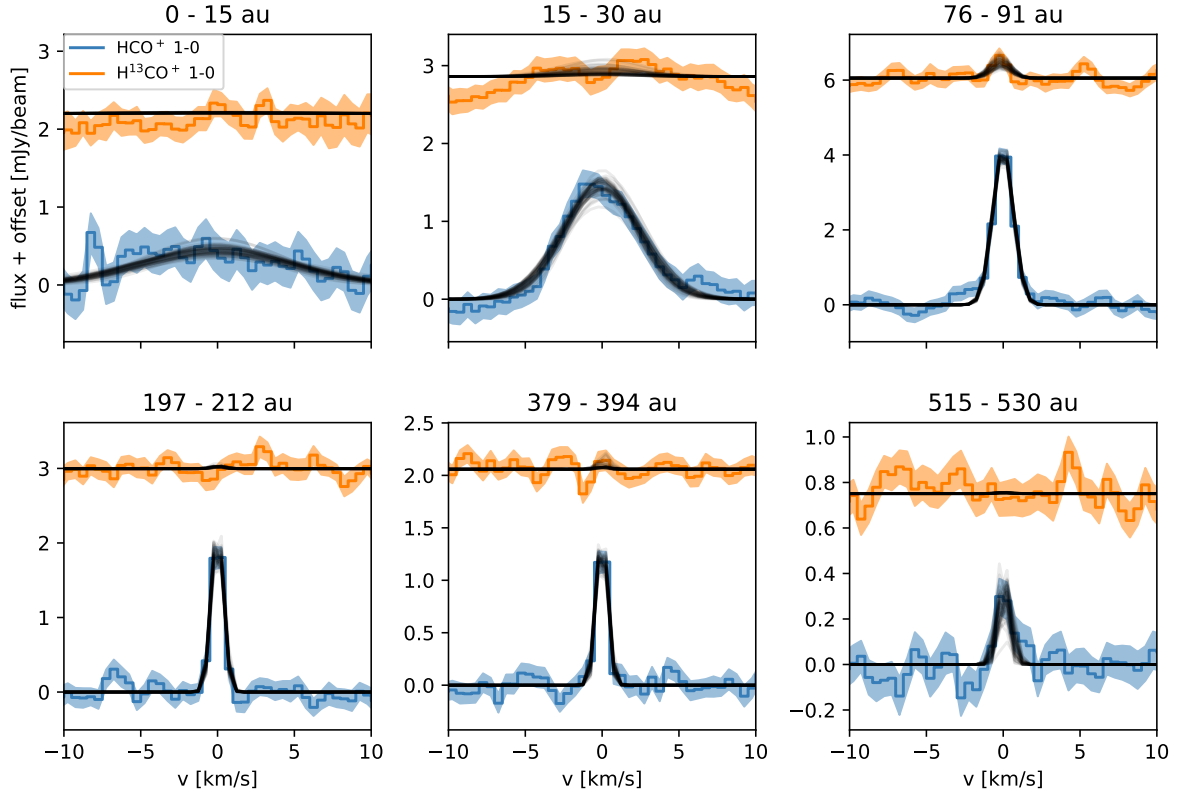


Figure 4. Examples of HCO^+ and H^{13}CO^+ $J = 1 - 0$ model spectra fit to azimuthally averaged spectra of HD 163296 for a few radial bins. The orange and blue solid lines show the data, with the shaded regions corresponding to the 1σ uncertainty. The black curves show 50 randomly selected models drawn from the Monte Carlo chain, with the selection probability being proportional to the posterior probability of the model. Spectra are vertically offset for clarity.

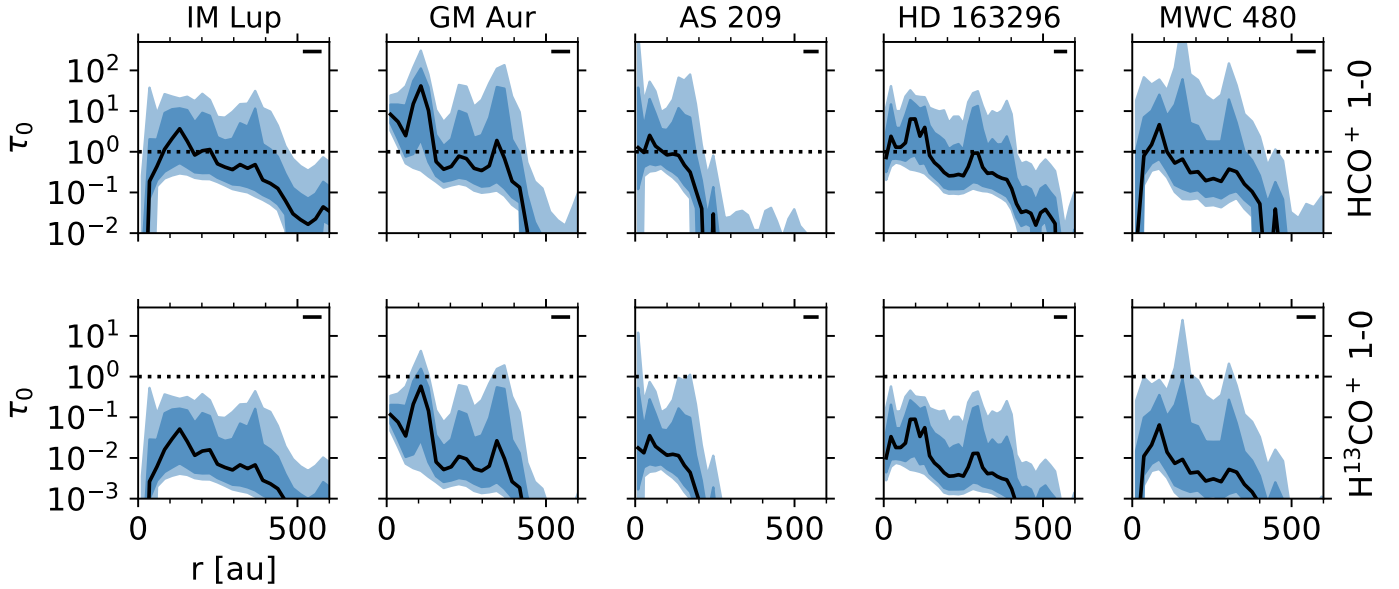


Figure 5. Optical depth profiles of HCO^+ ($J = 1 - 0$) and H^{13}CO^+ ($J = 1 - 0$) derived from fitting azimuthally averaged spectra. The black lines show the median of the posterior probability, while the shaded regions extend between the 16th to 84th and the 2.3th to 97.7th percentiles. The beam size is shown as a horizontal line in the upper right.

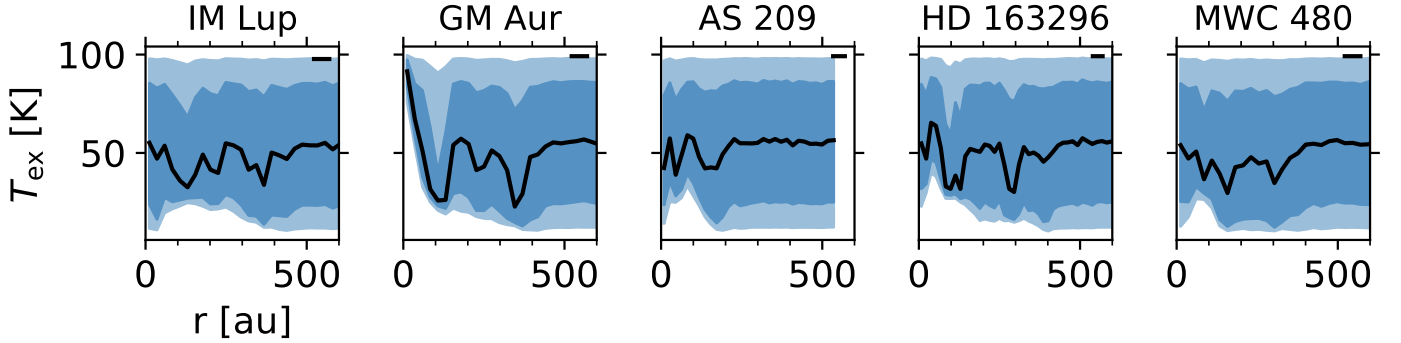


Figure 6. The excitation temperature derived from fitting azimuthally averaged spectra. The black lines show the median of the posterior probability, while the shaded regions extend between the 16th to 84th and the 2.3th to 97.7th percentiles. The beam size is shown as a horizontal line in the upper right.

in most of the disk radii. Exceptions are the innermost and outermost radii; at these radii, the C^{18}O line fluxes have relatively large uncertainties, and the error of the CO column density is 1 sigma. They also derived the CO column densities using the $J = 2 - 1$ transition of ^{13}CO , and $J = 1 - 0$ transition of ^{13}CO , C^{18}O , and C^{17}O , which are in reasonable agreement with the value based on C^{18}O ($J = 2 - 1$).

Overall, the radial profile of the HCO^+ column density is similar to that of CO. The panels in the middle row of Figure 7 show the column density ratio $N(\text{HCO}^+)/N(\text{CO})$. Since the CO column density was calculated on a finer radial grid than HCO^+ , we interpolated the CO column density at the radii of HCO^+ . The error bars in the middle panels reflect only the error of HCO^+ column density, which dominates over that of CO column density. The ratio is mostly within $10^{-5} - 10^{-4}$ at $\sim 100 - 500$ au, which suggests a close chemical link between these species, as expected from chemical models (e.g. Aikawa et al. 2015; Teague et al. 2015).

In the disk of IM Lup, the column densities of both HCO^+ and CO increase from $R \sim 500$ au to 100 au, where the HCO^+/CO column density ratio is remarkably constant. The HCO^+ column density then declines at $\lesssim 100$ au, while the CO column density becomes flat and rises inwards at $\lesssim 50$ au. In the GM Aur disk, the HCO^+/CO column density ratio exceeds 10^{-4} outside the dust continuum edge. Both the HCO^+ and CO column densities increase inwards up to ~ 100 au, while they have small local humps. At $R \sim 60$ au, the CO column density has a local maximum, while that of HCO^+ has a local minimum. This coincidence needs to be taken with caution, however, since the beam size of HCO^+ data is two times larger than that of CO, and since the column density estimates at the innermost radii suffers line broadening due to the velocity gradient within a beam. In the disk of AS 209, the radial profile of HCO^+ significantly differs from that of CO at $R \lesssim 100$ au. While the CO column density shows a broad depression at $R \sim 45 - 120$ au, the HCO^+ column density increases inwards up to ~ 75 au, and stays constant at inner radii within the error bars. In the disk around HD 163296, the column density ratio of HCO^+/CO decreases inwards up to $R \sim 240$ au, which corresponds to the edge of the millimeter dust continuum. From 240 au to 65 au, the ratio stays constant or has a shallow rise, while both the CO and HCO^+ column densities increase inwards. Inside the radius of ~ 65 au, which coincides with the CO snow line in the thermo-chemical model, the HCO^+ column density is roughly constant, while the CO column density increases towards the center by more than an order of magnitude. The sharp rise of CO column density and relatively flat distribution of HCO^+ column density inside the CO snow line is also seen in MWC 480, while the overall column density ratio of HCO^+/CO is slightly lower than that in HD 163296. We note that the X-ray spectrum of MWC 480 is significantly softer than that of HD 163296 (Dionatos et al. 2019). Since X-rays are the major ionization source in the molecular layer (see §4.3), the relatively low HCO^+/CO column density ratio in MWC 480 could be due to the lack of high energy X-rays (\gtrsim a few keV).

4. DISCUSSION

4.1. HCO^+ abundance in the warm molecular layers

In the molecular layers of protoplanetary disks, the major molecular ions are H_3^+ , HCO^+ and N_2H^+ , among which H_3^+ cannot be observed at millimeter wavelengths. Its deuterated counterpart o- H_2D^+ has not been detected so far (e.g. Chapillon et al. 2011). Figure 8 shows the radial profiles of the HCO^+ , N_2H^+ , and N_2D^+ column densities

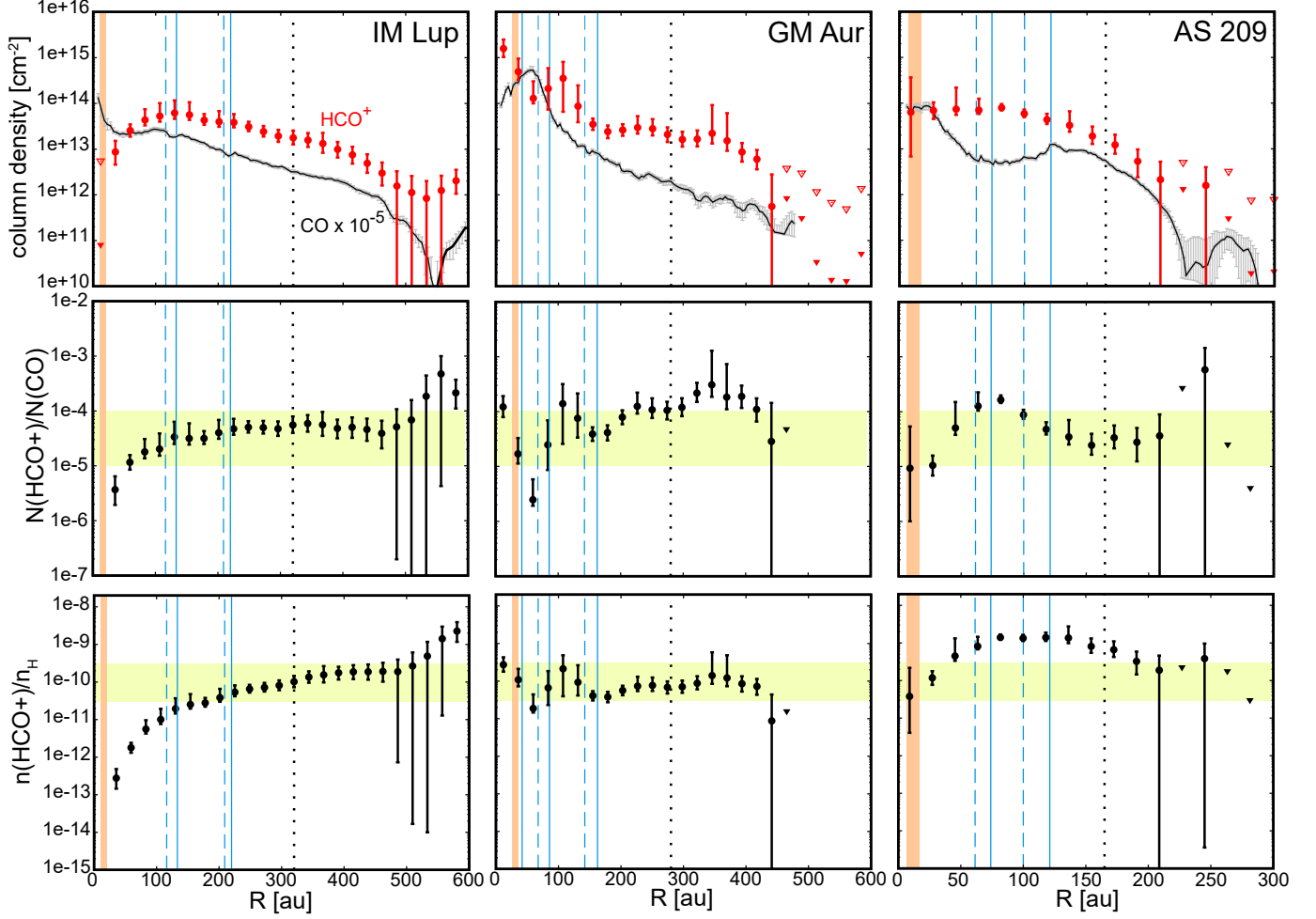


Figure 7. (Top) Column densities of HCO⁺ (red) and CO column density scaled by 10⁻⁵ (black lines with gray error bars). The error bars correspond to 10 % or 1 σ for CO (see §3.2), while they show the 16th and 84th percentile for HCO⁺. At radii where the median value of the molecular column density is lower than the value at 16th percentile by a factor of > 10 , we plot the upper limits as inverted triangles (84 percentile for closed triangles and 98 percentile for open triangles). The vertical orange bars mark the CO snowline as inferred from the model by Zhang & MAPS team (2021) with error of ± 5 au. The blue solid and dashed lines depict the radius of rings and gaps, respectively, in dust continuum. The black dotted lines depict the outer edge of the millimeter dust continuum. (Middle) The column density ratio of HCO⁺ to CO. The yellow bars mark the HCO⁺/CO column density ratio of $10^{-5} - 10^{-4}$. (Bottom) Abundance of HCO⁺ relative to hydrogen nuclei in the CO gas rich layer. The yellow bars mark the abundance of $3 \times 10^{-11} - 3 \times 10^{-10}$. In the middle and bottom panels, we consider only the error in HCO⁺ column density, since it dominates over the error of CO column density estimates. At radii where the median value of the HCO⁺ column density is lower than the value at 84th percentile by a factor of > 10 , we plot the value which corresponds to the 1- σ upper limit (i.e. 84 percentile of HCO⁺ column density) with an inverted triangle.

obtained in this work and by Cataldi & MAPS team (2021). We can see that HCO⁺ has the largest column densities among the observable molecular ions in our five disks.

HCO⁺ is expected to be the major molecular ion in the warm molecular layer where CO gas is abundant. Thus, here we assume that the majority of HCO⁺ coexists with CO in the warm molecular layer, and derive the HCO⁺ abundance there, based on the HCO⁺ to CO column density ratio. Furthermore, we assume that the CO abundance relative to hydrogen nuclei is equal to its canonical abundance in molecular clouds, 5.0×10^{-5} , multiplied by the CO depletion factor derived in Zhang & MAPS team (2021). The bottom panels in Figure 7 show the estimated HCO⁺ abundance. Since the uncertainty (error) of the HCO⁺ column density dominates over the that of the CO column density at most disk radii, and since the methods of error estimation are different between HCO⁺ and CO, we evaluate

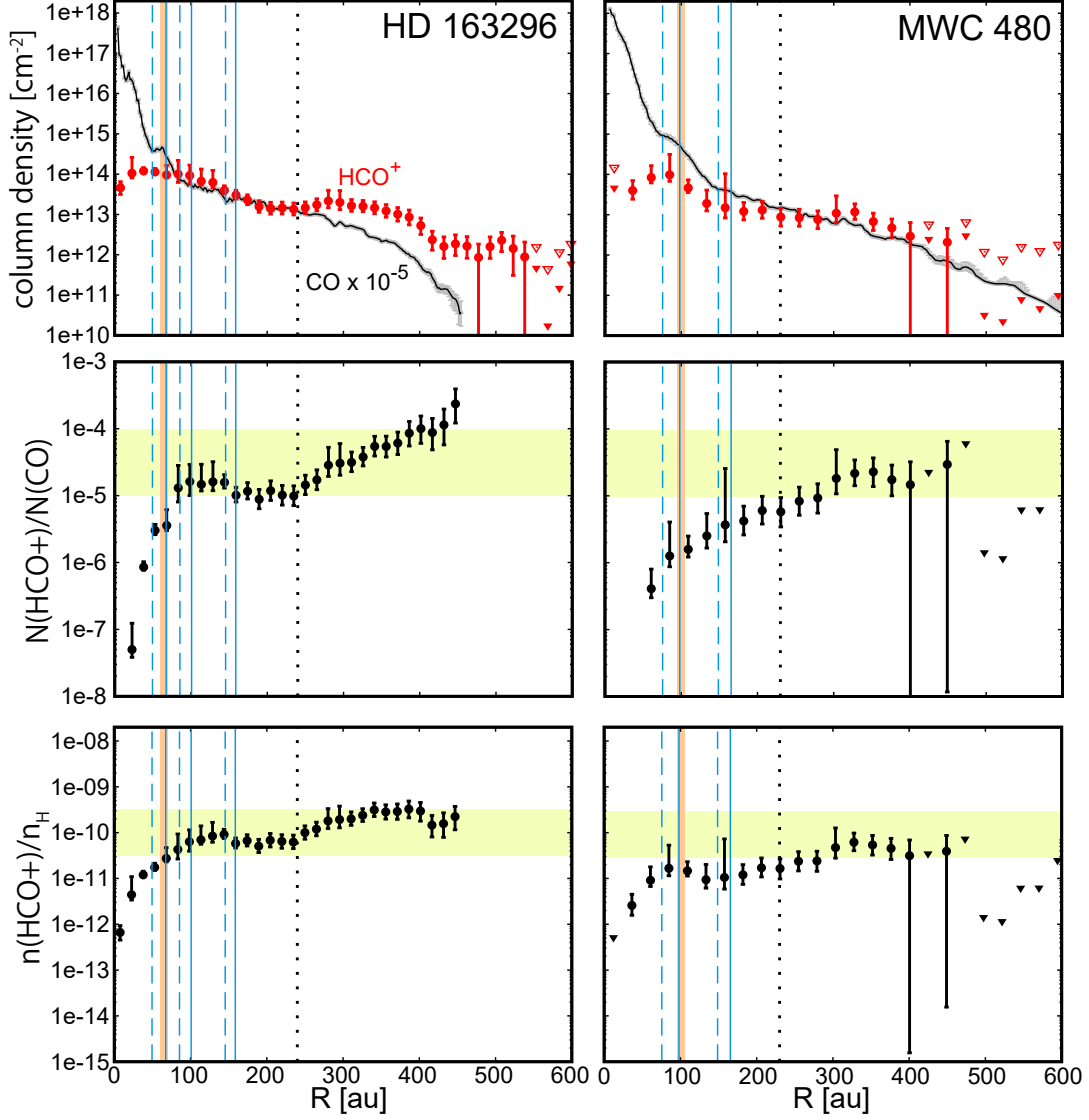


Figure 7. (cont)

the error of the HCO^+ abundance considering only that of the HCO^+ column density. Overall, the HCO^+ abundance is in a range of $3 \times 10^{-11} - 3 \times 10^{-10}$ outside ~ 100 au, and tends to decline towards the disk center at the inner radii.

In those inner regions, the CO-rich molecular layer extends towards the midplane, although detailed analysis by Zhang & MAPS team (2021) shows that the gaseous CO fractional abundance does not necessarily recover its canonical value (i.e. 10^{-4} relative to H_2) even inside of the CO snow line. Closer to the midplane, the gas density is higher and the ionization degree, i.e. the HCO^+ abundance, should be lower. Furthermore, HCO^+ is suppressed by grain-surface recombination (i.e. collision with a negatively charged grain), which could be more efficient than the recombination in the gas phase at high densities. The HCO^+ abundance averaged over the CO gas rich layer should thus be lower around and inside the CO snow line than at outer radii (see §4.3).

Although HCO^+ is expected to be one of the major molecular ions in the warm molecular layer, it is not always the most abundant ion. The relative abundances of major molecular ions, H_3^+ , HCO^+ , and N_2H^+ , are determined by the balance between proton transfer and recombination of relevant species, i.e. H_2 , CO , and N_2 (Aikawa et al. 2015). Furthermore, if the abundance of small grains is low enough to allow significant penetration of UV radiation, atomic

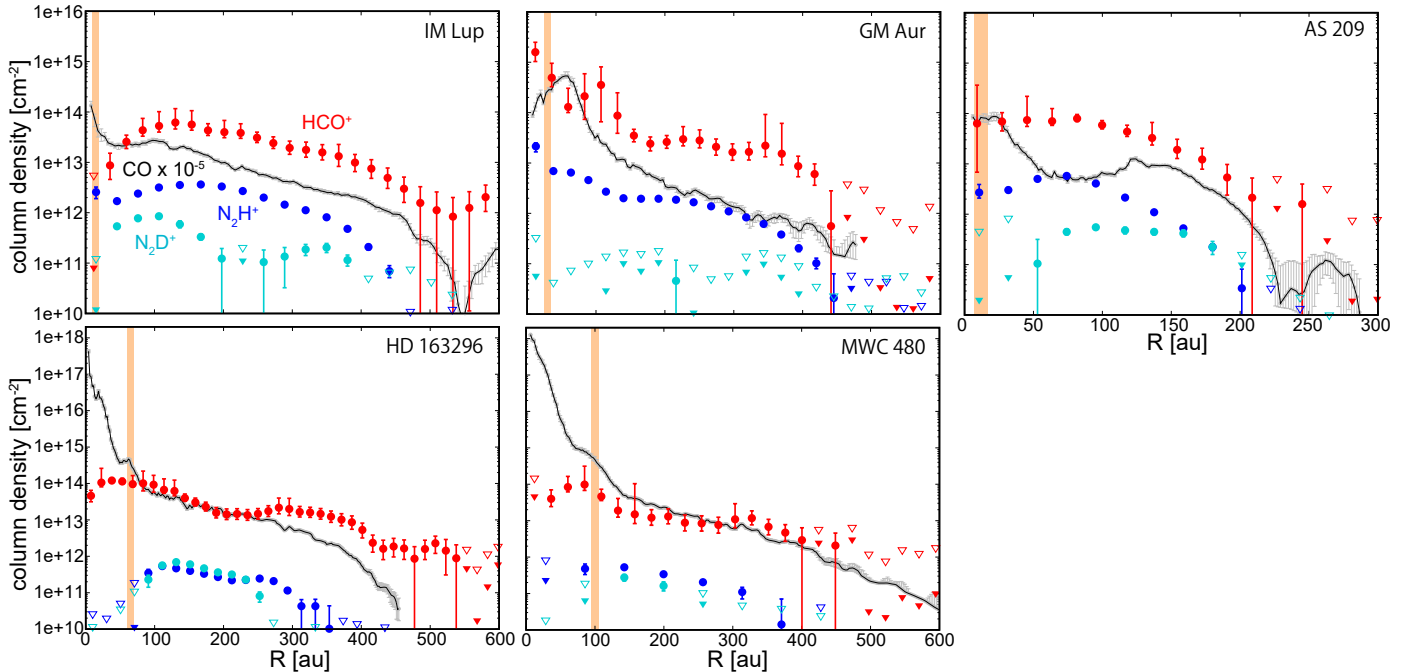


Figure 8. Column densities of HCO^+ (red), N_2H^+ (blue), and N_2D^+ (light blue). Black lines with gray error bars depict the CO column density scaled by 10^{-5} . The error bars corresponds to 10 % or 1σ for CO (see §3.2), while they show the 16th and 84th percentile for other species. At radii where the median value of the molecular column density is lower than the value of the 16th percentile by a factor of > 10 , we plot the upper limits as inverted triangles (84th percentile for closed triangles and 98th percentile for open triangles). The vertical orange bars mark the CO snowline as inferred from the model by Zhang & MAPS team (2021).

ions such as C^+ and S^+ can dominate even in the CO rich layers (e.g. Aikawa et al. 2015). Therefore, the HCO^+ abundance derived here should be considered as a lower limit of the ionization degree in the molecular layer.

4.2. HCO^+ enhancement in gas gaps

The HCO^+ abundance exceeds 10^{-9} at $50 \text{ au} \lesssim R \lesssim 150 \text{ au}$ in AS 209, where the CO column density shows a depression. Favre et al. (2019) observed $\text{DCO}^+ J = 3 - 2$ in AS 209 with high resolution ($0''.26 \times 0''.21$) and found a ring-like emission with its peak at $\sim 85 \text{ au}$. They suggest that the over-density of DCO^+ is caused by the more efficient ionization at the radius of gas and dust depletion, which is carved by a planet of $\lesssim 0.3 M_{\text{Jup}}$ at $\sim 100 \text{ au}$. The high HCO^+ abundance at $50 \text{ au} \lesssim R \lesssim 150 \text{ au}$ is consistent with their scenario.

Alarcón & MAPS team (2021), on the other hand, calculated the thermal structure in two disk models for AS 209; model A assumes a smooth gas distribution and a CO abundance drop around $R \sim 80 \text{ au}$, while model B assumes a constant CO abundance combined with a gas density drop around 80 au . They found that the radial pressure profile derived by Teague et al. (2018b) is shallower than in model B, and concluded that the CO column density drop at 80 au is caused mainly by a CO abundance drop rather than a gas density drop. Self-consistent modeling of the thermal structure and the HCO^+ and DCO^+ chemistry would be useful to distinguish between these scenarios.

We also note correlated local enhancements of HCO^+ and DCO^+ in HD 163296. Flaherty et al. (2017) observed $\text{DCO}^+ (J = 3 - 2)$ with a beam of $0.5'' \times 0.59''$ and found that DCO^+ emission is confined to three concentric rings at $54, 124,$ and 214 au . The ring at 124 au is the brightest and coincides with the shoulder seen in HCO^+ emission in Figure 3 and the local enhancement of the HCO^+/CO column density ratio (Figure 7). Teague et al. (2018a) analyzed the disk gas kinematics around HD 163296 and found deviations from Keplerian rotation, which suggests the presence of a $1 M_{\text{Jup}}$ planet at 83 au and a $1.3 M_{\text{Jup}}$ planet at 137 au . Hydrodynamic models of the HD 163296 disk with these planets show gas gaps (i.e. gas density decrease) around the planet orbits. The local enhancement of DCO^+ and HCO^+ around 125 au could be related to such gas gaps.

In MWC 480, the CO column density shows a local minimum around the gap seen in dust continuum at ~ 76 au (Figure 7). We note that the HCO^+ column density has a local maximum at this radius; we derived the column density distribution with radial grids of a quarter of the beam size to confirm the coincidence. It again suggests a correlation between gas gap and HCO^+ enhancement. Observations of HCO^+ with higher angular resolution are desirable for further studies.

4.3. Constraining the ionization structure with a template disk chemistry model

MAPS observations, as well as previous ALMA observations of disks in the last few years, show that detailed physical structure, e.g. size, flaring, and temperature structure vary significantly among disks (e.g. Law & MAPS team 2021b). While source-specific modeling is desirable, it is out of the scope of the present work. However, we note that the derived abundance and its radial distribution of HCO^+ have common features; the HCO^+ abundance is $\sim 3 \times 10^{-11} - 3 \times 10^{-10}$ at $\gtrsim 100$ au, while it tends to decrease inwards at smaller radii. These features should reflect the basic chemistry of HCO^+ , which is not very sensitive to the details of the disk structure. Therefore, we compare our results with some template disk models.

We adopt the disk chemistry model of Aikawa et al. (2018); the disk mass is $1.7 \times 10^{-2} M_{\odot}$ and the mass of the central star is $0.5 M_{\odot}$. Stellar UV and X-ray luminosities are 10^{31} erg s^{-1} and 10^{30} erg s^{-1} , respectively. While the dust sedimentation is not considered, the maximum grain size is set to be 1 mm. Since the total gas-to-dust mass ratio is set to be the same as the interstellar value (~ 100), the abundance of small dust grains is reduced compared with the interstellar dust. The 2D (R, Z) distributions of the gas number density (i.e. number density of hydrogen nuclei n_{H}) and temperature are shown in Figure 19 in Appendix E. While Aikawa et al. (2018) varied several parameters in the calculation of the chemistry model, we here show three models: their fiducial model, a high C/O model, and a low ζ model, which is newly calculated for the present work. The fiducial model is a static disk model with a cosmic-ray ionization rate of $5 \times 10^{-17} \text{ s}^{-1}$. Two other ionization sources, X-rays and the decay of SLR are included in the model with the X-ray spectrum of TW Hya and the ionization rate by SLR of $\zeta_{\text{SLR}} = 1 \times 10^{-18} \text{ s}^{-1}$. The initial molecular abundance for the disk chemistry is set by calculating the chemical evolution from the molecular cloud formation stage to the collapse of a star-forming core. In the fiducial model, the elemental abundance of C and O are 7.82×10^{-5} and 1.8×10^{-4} relative to hydrogen nuclei (i.e. C/O=0.43). Disk observations in recent years, however, suggest low C/H ratios and high C/O ratios in the gas phase (e.g. Bergin et al. 2014, 2016; Zhang & MAPS team 2021; Bosman & MAPS team 2021). This is likely due to the removal of ice by the sedimentation and radial migration of ice-coated pebbles (Kama et al. 2016; Krijt et al. 2018). Thus, in the high C/O model, H_2O is completely removed and CO is reduced by one order of magnitude in the initial molecular abundances, which results in a C/O ratio of 1.43. In addition to these two models, we run a low ζ model, in which the cosmic-ray ionization rate is set to zero. Ionization rates by X-ray and SLR are set to be the same as in the fiducial model, and the initial molecular abundance is the same as the high C/O model. Since we aim to constrain the ionization rate rather than identifying the main ionization source, the low ζ model can simply be considered as a model with a midplane ionization rate of $\zeta_{\text{mid}} = 10^{-18} \text{ s}^{-1}$, while ζ_{mid} is $5 \times 10^{-17} \text{ s}^{-1}$ in the fiducial model and high C/O model.

While molecular evolution in the disk is calculated up to $t = 1 \times 10^6$ yr, we compare our observational results with the molecular abundances at $t = 1 \times 10^5$ yr, which is comparable to the vertical mixing timescale at the radius of several tens of au assuming an α parameter of 10^{-3} for turbulent mixing (e.g. Aikawa et al. 1996). In gas-grain chemical networks, volatile species tend to be converted to less volatile ices. At $t = 10^6$ yr, a significant amount of CO and N_2 is converted to CO_2 , CH_3OH , and NH_3 , which could be an artifact of the static disk assumption (i.e. without mixing or accretion). The desorption rate and thermal diffusion rate (and thus the reaction rate) on the grain surface are very sensitive to temperature. In the static model, in which gas and dust stay at the same position, and thus are kept at a constant temperature, only a limited number of species can effectively diffuse and react, which results in an accumulation of specific products. At $t = 1 \times 10^5$ yr, such accumulations are less significant (see Aikawa et al. 2015, for more details).

Figure 9 shows the abundances of CO, HCO^+ , and electrons relative to hydrogen nuclei, in the low ζ model. The abundances in the other models are shown in Figure 19 in Appendix E. We can see that CO and HCO^+ are mostly co-spatial and that the observed features are reproduced; the HCO^+/CO abundance ratio is $\sim 10^{-5} - 10^{-4}$, and the HCO^+ abundance is $\sim 10^{-10}$ in the lower part of the CO-rich layer, where the density is higher. In Figure 9, the dashed line depicts the CO snow surface and the dotted lines depict the position where the X-ray ionization rate is $5 \times 10^{-17} \text{ s}^{-1}$ (upper), $1 \times 10^{-18} \text{ s}^{-1}$ (middle), and $1 \times 10^{-19} \text{ s}^{-1}$ (lower). We note that the dashed line and dotted

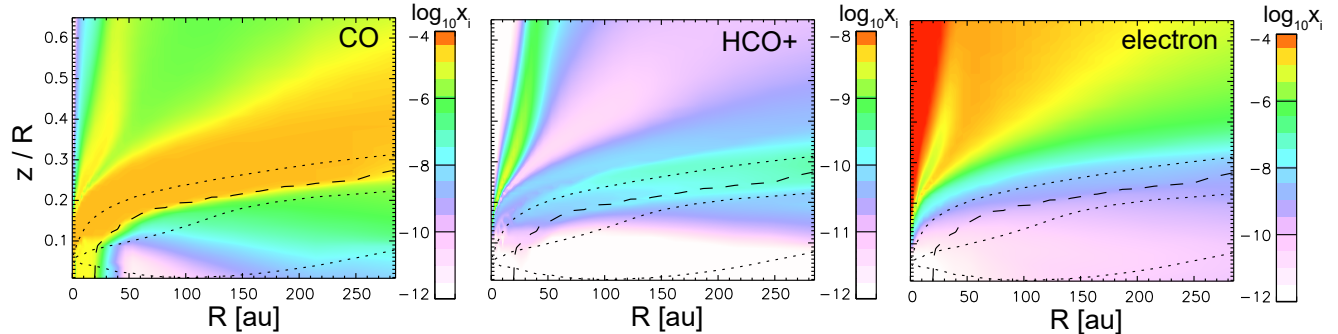


Figure 9. The abundances of CO (left), HCO^+ (middle), and electrons (right) relative to hydrogen nuclei in the low ζ model. The dashed line depicts the CO snow surface and the dotted lines show the positions where the X-ray ionization rate is $5 \times 10^{-17} \text{ s}^{-1}$ (the upper dotted line), $1 \times 10^{-18} \text{ s}^{-1}$ (the middle dotted line), and $1 \times 10^{-19} \text{ s}^{-1}$ (the lower dotted line),

lines are roughly parallel at radii > 50 au, probably because both parameters are controlled by the radiation transfer from the central star (i.e. stellar irradiation and X-rays). Inside the CO snow line (where the dashed line crosses the midplane), CO is indeed abundant near the midplane, although its abundance is reduced by an order of magnitude compared to the initial value ($\sim 10^{-5}$) due to the conversion to less volatile species such as CO_2 ice. In this region, the HCO^+/CO abundance ratio is less than 10^{-5} in the low ζ model, which is also consistent with the observations. Comparing the HCO^+ and the electron abundances, we can see that the former is slightly lower than the latter even in the layers where the HCO^+ abundance peaks. This means that the ionization degree is actually higher than the HCO^+ abundance; atomic ions are relatively abundant even in the CO-rich layer in the model.

Figure 10 shows the radial profiles of the column densities of CO (multiplied by 10^{-5}), HCO^+ , N_2H^+ , and N_2D^+ in the three models. As references, 2D distributions of absolute abundances (i.e. number densities) of major molecular ions in the low ζ model are shown in Figure 11. Similar plots for the other two disk models are shown in Figure 20 in Appendix E. The column densities in the models are almost constant outside ~ 100 au, while the observed values decline outwards. This discrepancy might arise because the model gas density is not exponentially tapered, but simply follows a power law up to a radius of 284 au. We thus only compare the model column densities inside ~ 200 au with the observed values. In all three models, the radial profile of the column density ratio $N(\text{HCO}^+)/N(\text{CO})$ is similar to those in Figure 7; $N(\text{HCO}^+)/N(\text{CO})$ is nearly constant ($\sim 10^{-5}$), but declines towards the disk center inside a certain radius, which corresponds to the CO snow line in the disk models.

Figure 10 shows that at radii outside the CO snow line (~ 20 au in the template model) the HCO^+ column density is not sensitive to ζ_{mid} , since the contribution of the X-ray ionized region is significant in the CO-rich layer there (see Figure 11 and Figure 20). Inside the CO snow line, the CO-rich layer extends to the midplane. The HCO^+ column density and the gas column density ratio $N(\text{HCO}^+)/N(\text{CO})$ around and inside the CO snow line is thus more sensitive to ζ_{mid} .³ The peak value of the HCO^+ column density is lower in the low ζ model than in the models with $\zeta_{\text{mid}} = 5 \times 10^{-17} \text{ s}^{-1}$ by a factor of 4.6 (fiducial model) and 4.2 (high C/O model). The column density ratio of HCO^+/CO at the HCO^+ column density peak is also lower in the low ζ model accordingly. Around the CO snow lines predicted from the thermo-chemical model of Zhang & MAPS team (2021), the HCO^+ column density derived from the observation is $\gtrsim 10^{14} \text{ cm}^{-2}$ with the column density ratio of $\text{HCO}^+/\text{CO} \sim 10^{-5}$ in our targeted disks, as in our fiducial model or high C/O model, except for those around IM Lup and MWC 480. It may suggest $\zeta_{\text{mid}} \sim 10^{-17} \text{ s}^{-1}$ around the CO snow line. We note, however, that the HCO^+ column density would also depend on the total gas column density, which is not varied in the set of template models shown here. While the mass of the template disk model is within the range of estimated values for GM Aur and IM Lup, AS 209 is less massive and the disks around the Herbig Ae stars are more massive (Zhang & MAPS team 2021) (see §4.4). Source-specific models are needed for further comparison.

³ We note that the absolute abundance of HCO^+ in the midplane is high even at radii slightly outside the CO snow line. For HCO^+ to be the abundant ion, CO does not need to fully sublimate to the gas phase (Aikawa et al. 2015).

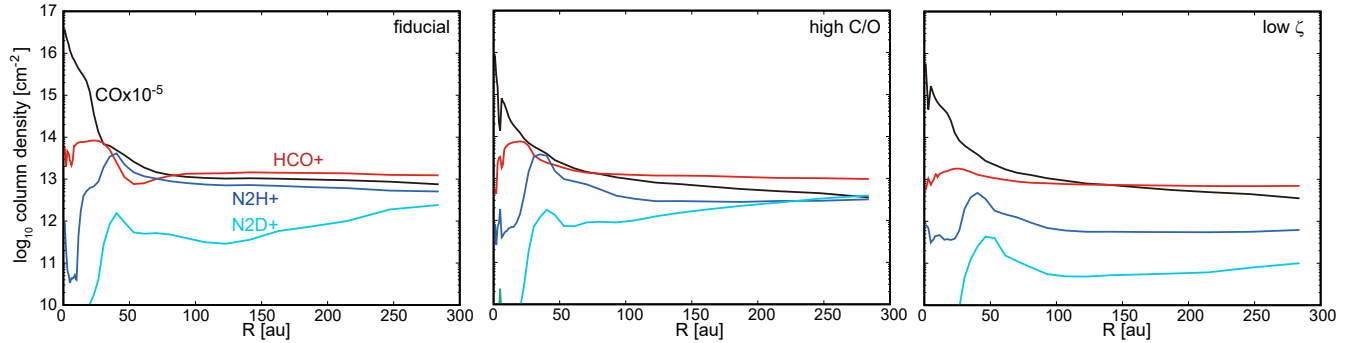


Figure 10. Column densities of CO (multiplied by 10^{-5}), HCO^+ , N_2H^+ , and N_2D^+ in the fiducial model (left), high C/O model (middle) and low ζ model (right).

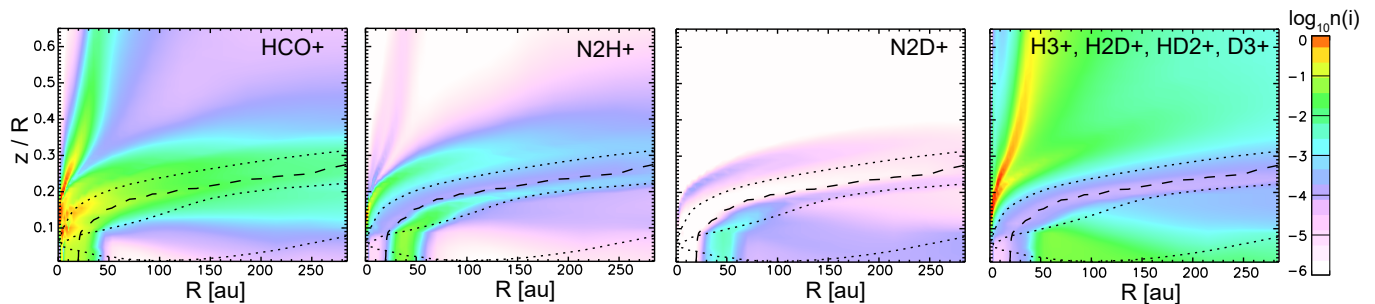


Figure 11. The absolute abundances (number densities) of HCO^+ , N_2H^+ , N_2D^+ , and H_3^+ (and its deuterated isotopomers) relative to hydrogen nuclei in the low ζ model. The dashed line depicts the CO snow surface and the dotted lines depict the position where the X-ray ionization rate is $5 \times 10^{-17} \text{ s}^{-1}$ (the upper dotted line), $1 \times 10^{-18} \text{ s}^{-1}$ (the middle dotted line), and $1 \times 10^{-19} \text{ s}^{-1}$ (the lower dotted line),

4.4. Ionization rate traced by N_2H^+ and N_2D^+

The template disk models (Figures 10, 11, and 20) indicate that, in contrast to HCO^+ , the column densities of N_2H^+ and N_2D^+ are more sensitive to the ionization rate below the CO snow surface, where these molecular ions are relatively abundant. In the cold midplane, H_3^+ and its deuterated isotopomers are the most abundant ions, but H_3^+ and D_3^+ are not observable at radio wavelengths, and H_2D^+ and HD_2^+ are not detected so far, possibly due to unfavorable o/p ratios (e.g. Chapillon et al. 2011). Figure 20 shows that among the observable molecular ions, N_2D^+ is the best proxy of deuterated H_3^+ and thus the best probe of ionization rate in the midplane. Although its abundance is lower than the sum of H_3^+ and its deuterated isotopomers, the gas above the CO snow surface does not significantly contribute to its column density in our template disk models. In the template disk models, the N_2H^+ and N_2D^+ column densities have a peak around $R \sim 50$ au, where these molecular ions are abundant in the midplane (see also Qi et al. 2019). This indicates that ζ_{mid} could be best investigated by their peak column densities, especially by the N_2D^+ column density.

The column densities of N_2H^+ and N_2D^+ in our target disks are derived by Cataldi & MAPS team (2021) and are plotted in Figure 8. As expected from the template disk models, these column densities have a peak outside the CO snow line, except for GM Aur, for which the N_2H^+ column density is the highest at the innermost radial grid. The value at the innermost grid could, however, be overestimated, since these column densities are derived by assuming a fixed excitation temperature of 20 K. When the excitation temperature is set to be the same as the midplane temperature of the thermochemical model of Zhang & MAPS team (2021), the N_2H^+ column density has a peak ($\sim 10^{13} \text{ cm}^{-2}$) around $R \sim 100$ au (Cataldi & MAPS team 2021).

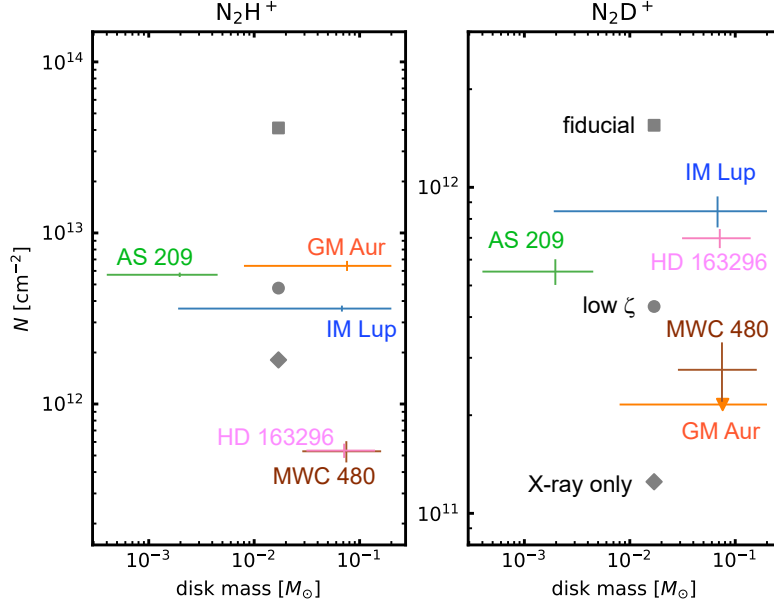


Figure 12. The N_2H^+ and N_2D^+ column densities as a function of disk mass. For each disk, a mass range adopted from Zhang & MAPS team (2021) is shown as horizontal error bar. The column densities correspond to the peak values, with the error bars indicating the 16th and 84th percentiles. For N_2D^+ in GM Aur, we instead plot the 99.85th percentile at ~ 100 au as an upper limit. Predictions from the template models are shown by the gray points.

Unlike HCO^+ , the distributions of N_2H^+ and N_2D^+ are expected to anti-correlate with that of CO. We thus consider their column densities rather than the column density ratio to CO. In Figure 12, we plot the peak N_2H^+ and N_2D^+ column densities derived by Cataldi & MAPS team (2021) versus disk mass to see if there is any trend. For each disk, a range of possible masses is shown, extending from the minimum masses to the best-fit mass given in Tables 3 and 2 of Zhang & MAPS team (2021), respectively. While the estimated disk masses of IM Lup, GM Aur, HD 163296, and MWC 480 overlap with each other⁴, their N_2H^+ and N_2D^+ peak column densities vary, which indicates that the midplane ionization rate varies among the disks. The gray squares and circles depict the peak column densities around $R \sim 50$ au in the fiducial model and low ζ model, respectively. The gray diamonds show the values in the model with X-ray ionization only; i.e. the midplane ionization rate is $\lesssim 10^{-19} \text{ s}^{-1}$. The peak column densities of the high C/O model are not plotted but are similar to those of the fiducial model.

The N_2H^+ column densities of IM Lup, GM Aur, and AS 209 indicate $\zeta_{\text{mid}} \sim 10^{-18} \text{ s}^{-1}$. For MWC 480 and HD 163296, the N_2H^+ column density is lower than that of the X-ray only model, which indicates that the X-ray ionization is less effective in these disks than in our template models. We note that a fraction of N_2H^+ exists in the layer with relatively high X-ray ionization rate ($\gtrsim 5 \times 10^{-17} \text{ s}^{-1}$), which sets the floor value of the N_2H^+ column density in our template models. For MWC 480, the low N_2H^+ column density is consistent with its soft X-ray spectrum and relatively low HCO^+ column density. Alternative explanation for the variety of N_2H^+ column density would be the temperature structure in the disk. The column density of N_2H^+ should be lower if the midplane layer of the low temperature ($\lesssim 20 \text{ K}$) is thinner (Qi et al. 2019). This could be the case for MWC 480 disk, in which both N_2H^+ and N_2D^+ column densities are low. HD 163296, on the other hand, has relatively high column density of N_2D^+ , which indicate that there are plenty of cold gas in the midplane (see below).

The N_2D^+ peak column densities of IM Lup, AS 209, and HD 163296 are similar to or slightly larger than the value from the low ζ model, which suggests $\zeta_{\text{mid}} \gtrsim 10^{-18} \text{ s}^{-1}$. In the HD 163296 disk, the peak N_2D^+ column density is relatively high, while the low N_2H^+ column density indicates lower X-ray ionization rate than the template models. The midplane ionization rate, which is better traced by N_2D^+ , would thus be set by SLR or high energy particles. In GM Aur, on the other hand, the upper limit of N_2D^+ column density indicates a low ionization rate ($< 10^{-18} \text{ s}^{-1}$) in the midplane.

⁴ Fedele et al. (2018) reproduced their 1.3 mm dust continuum image with a disk model with a dust mass of $3.5 \times 10^{-4} M_{\odot}$. If the gas/dust mass ratio is 100, the disk mass of AS 209 is also similar to the disk mass of IM Lup and GM Aur.

Finally we note that the N_2H^+ and N_2D^+ column densities depend not only on ζ_{mid} , but also on other parameters such as the vertical temperature distribution and the disk mass (Cleeves et al. 2014; Qi et al. 2019). Source specific models are needed to estimate the midplane ionization rate more quantitatively for each object.

5. CONCLUSIONS

We observed and analyzed $\text{HCO}^+ J = 1 - 0$ and $\text{H}^{13}\text{CO}^+ J = 1 - 0$ lines towards the protoplanetary disks around IM Lup, GM Aur, AS 209, HD 163296, and MWC 480. $\text{H}^{13}\text{CO}^+ J = 1 - 0$ was detected in all five disks, while $\text{H}^{13}\text{CO}^+ J = 1 - 0$ was detected ($\text{SNR} > 6\sigma$) towards GM Aur and HD 163296 and tentatively detected ($\text{SNR} > 3\sigma$) towards the other disks by a matched filter analysis in the uv plane. The disk-integrated flux of $\text{H}^{13}\text{CO}^+ J = 1 - 0$ is also above 3σ in IM Lup, GM Aur, and HD 163296.

We derived the HCO^+ column density by fitting the azimuthally averaged spectra of HCO^+ and H^{13}CO^+ simultaneously for radial bins of half the beam FWHM. In all five disks, the HCO^+ column density increases inwards, but becomes flat or drops towards the center inside a radius of $R \sim 100$ au. The column density ratio of $N(\text{HCO}^+)/N(\text{CO})$ is about $10^{-5} - 10^{-4}$ at $R \gtrsim 100$ au, except for the MWC 480 disk, in which the column density ratio is $< 10^{-5}$ at $R \lesssim 200$ au.

We derived the HCO^+ abundance in the warm CO-rich layer, where HCO^+ is expected to be the dominant molecular ion, via the column density ratio $N(\text{HCO}^+)/N(\text{CO})$ using the radial profiles of CO column density and CO depletion factor from Zhang & MAPS team (2021). Beyond ~ 100 au, the derived HCO^+ abundance ranges from $3 \times 10^{-11} - 3 \times 10^{-10}$ in the IM Lup, GM Aur, HD 163296 disks. The HCO^+ abundance is lower in MWC 480, possibly due to the lack of high energy ($> \text{a few keV}$) X-rays. The HCO^+ abundance tends to decline at towards the disk center for $R \lesssim 100$ au. This can be explained by the lower ionization degree in denser gas, especially inside the CO snow line, where the CO-rich layer is in the midplane.

We find a hint of a correlation between the HCO^+ abundance and the gap carved by a putative planet in AS 209: the HCO^+ abundance exceeds 10^{-9} at $R \sim 50 - 150$ au, where the CO column density is depressed. This region seems to correspond to the gas gap, where ionization would be more efficient. In HD 163296, the HCO^+ abundance shows a shallow bump at $100 - 150$ au, which coincides with the radius of DCO^+ enhancement found by Flaherty et al. (2017). This feature could also be related to the enhanced ionization around a gas gap. In MWC 480, the HCO^+ column density has a local maximum at ~ 76 au, which coincides with the local depression of CO and the gap seen in the dust continuum.

Finally, we compared the column densities of HCO^+ , N_2H^+ , and N_2D^+ with those of template disk models: a fiducial disk model with a midplane ionization rate ζ_{mid} of $5 \times 10^{-17} \text{ s}^{-1}$, a model with CO and H_2O depletion, and a model with $\zeta_{\text{mid}} = 1 \times 10^{-18} \text{ s}^{-1}$. The almost constant HCO^+ abundance at $R \gtrsim 100$ au is explained by X-ray ionization in the CO-rich layer. The decline of the HCO^+ abundance at the inner radii, on the other hand, can be explained by CO sublimation inside the CO snow line; the CO-rich layer then extends to the midplane, where the ionization degree is low due to high density. While the estimated disk mass range of IM Lup, GM Aur, HD 163296, and MWC 480 overlap with each other, their peak column densities of N_2H^+ and N_2D^+ vary, which may indicate that the midplane ionization rate varies among disks. The peak N_2D^+ column density suggests a midplane ionization rate of $\gtrsim 10^{-18} \text{ s}^{-1}$ for IM Lup, AS 209, and HD 163296, while the upper limit of N_2D^+ column density indicates it is $< 10^{-18} \text{ s}^{-1}$ for GM Aur. The peak column density of N_2H^+ is lower in MWC 480 than in other disks, which is consistent with its soft X-ray spectrum and relatively low HCO^+ column density. Alternatively, the low column densities of N_2H^+ and N_2D^+ in the MWC 480 disk could be due to its warmer temperature; i.e. cold midplane layer is thinner than in other disks. Source-specific models are needed for further evaluation of the midplane ionization rate.

ACKNOWLEDGMENTS

This paper makes use of the following ALMA data: ADS/JAO.ALMA#2018.1.01055.L, ADS/JAO.ALMA#2015.1.00678.S, ADS/JAO.ALMA#2012.1.00681.S, ADS/JAO.ALMA#2015.1.00657.S. ALMA is a partnership of ESO (representing its member states), NSF (USA) and NINS (Japan), together with NRC (Canada), MOST and ASIAA (Taiwan), and KASI (Republic of Korea), in cooperation with the Republic of Chile. The Joint ALMA Observatory is operated by ESO, AUI/NRAO and NAOJ. This research has made use of NASA's Astrophysics Data System and the SIMBAD database, operated at CDS, Strasbourg, France.

We would like to thank the anonymous referee for careful reading of our manuscript and for constructive comments. Y.A. acknowledges support by NAOJ ALMA Scientific Research Grant code 2019-13B, Grant-in-Aid for Scientific Research (S) 18H05222, and Grant-in-Aid for Transformative Research Areas (A) 20H05844 and 20H05847. G.C. is supported by the NAOJ ALMA Scientific Research Grant code 2019-13B. Y.Y. is supported by IGPEES, WINGS Program, The University of Tokyo. K.Z. acknowledges the support of the Office of the Vice Chancellor for Research and Graduate Education at the University of Wisconsin – Madison with funding from the Wisconsin Alumni Research Foundation. S.M.A. and J.H. acknowledge funding support from the National Aeronautics and Space Administration under Grant No. 17-XRP17 2-0012 issued through the Exoplanets Research Program. E.A.B. and A.D.B. acknowledges support from NSF AAG Grant #1907653. L.I.C. gratefully acknowledges support from the David and Lucille Packard Foundation and Johnson & Johnson’s WiSTEM2D Program. V.V.G. acknowledges support from FONDECYT Iniciación 11180904 and ANID project Basal AFB-170002. J.D.I. acknowledges support from the Science and Technology Facilities Council of the United Kingdom (STFC) under ST/T000287/1. C.J.L. acknowledges funding from the National Science Foundation Graduate Research Fellowship under Grant No. DGE1745303. R.L.G. acknowledges support from a CNES fellowship grant. F.M. acknowledges support from ANR of France under contract ANR-16-CE31-0013 (Planet-Forming-Disks) and ANR-15-IDEX-02 (through CDP “Origins of Life”). H.N. acknowledges support by NAOJ ALMA Scientific Research Grant code 2018-10B and Grant-in-Aid for Scientific Research 18H05441. K.I.Ö. acknowledges support from the Simons Foundation (SCOL #321183) and an NSF AAG Grant (#1907653). R.T. acknowledges support from the Smithsonian Institution as a Submillimeter Array (SMA) Fellow. T.T. is supported by JSPS KAKENHI Grant Numbers JP17K14244 and JP20K04017. C.W. acknowledges financial support from the University of Leeds, STFC and UKRI (grant numbers ST/R000549/1, ST/T000287/1, MR/T040726/1). K.Z., K.R.S., J.H., J.B., J.B.B., and I.C. acknowledge the support of NASA through Hubble Fellowship grants HST-HF2-51401.001, HST-HF2-51419.001, HST-HF2-51460.001-A, HST-HF2-51427.001-A, HST-HF2-51429.001-A, and HST-HF2-51405.001-A awarded by the Space Telescope Science Institute, which is operated by the Association of Universities for Research in Astronomy, Inc., for NASA, under contract NAS5-26555.

Facilities: ALMA

Software: Astropy (Astropy Collaboration et al. 2013; Price-Whelan et al. 2018), bettermoments (Teague & Foreman-Mackey 2018), CASA (McMullin et al. 2007), emcee (Foreman-Mackey et al. 2013), gofish (Teague 2019), matplotlib (Hunter 2007), NumPy (van der Walt et al. 2011), pythonradex (<https://github.com/gica3618/pythonradex>), SciPy (Virtanen et al. 2020), SPECTCOL (VAMDC Consortium, <http://www.vamdc.org>), VISIBLE (Loomis et al. 2018).

APPENDIX

A. HYBRID ZEROth MOMENT MAPS WITH A 0''5 BEAM

While we used the data cubes tapered to a circular 0''3 beam for the analysis, faint emission is better recognized in images with lower spatial resolution. Since Band 3 lines tend to be fainter than Band 6 lines, the MAPS collaboration also produced the data cube tapered to a circular 0''5 beam for Band 3 lines (Öberg & MAPS team 2021; Czekala & MAPS team 2021). Figure 13 shows the hybrid zeroth moment maps of the $J = 1 - 0$ lines of HCO⁺ and H¹³CO⁺ tapered to a circular 0''5 beam. All maps were produced by combining a Keplerian mask and a smoothed 0σ -clip mask (Law & MAPS team 2021a).

B. MATCHED FILTER ANALYSIS AND DISK-INTEGRATED SPECTRA FOR H¹³CO⁺ $J = 1 - 0$

The $J = 1 - 0$ line of H¹³CO⁺ is not clearly seen in our zeroth moment maps (Figure 2), radial emission profiles (Figure 3), or azimuthally averaged spectra (Figure 16a). To test whether the line is detected, we applied a matched filter analysis in the uv plane (Loomis et al. 2018)(see also Czekala & MAPS team 2021). We calculate the visibilities of a Keplerian disk model, which are then cross-correlated with the observed visibilities to produce a response for each channel of the data. The response spectrum is then divided by the rms of the response spectrum at signal-free regions. Since we do not know the radial distribution of the emission, we computed the filter response for a series of Keplerian disk models with varying radial extents to find the Keplerian model that maximizes the SNR at the systemic velocity.

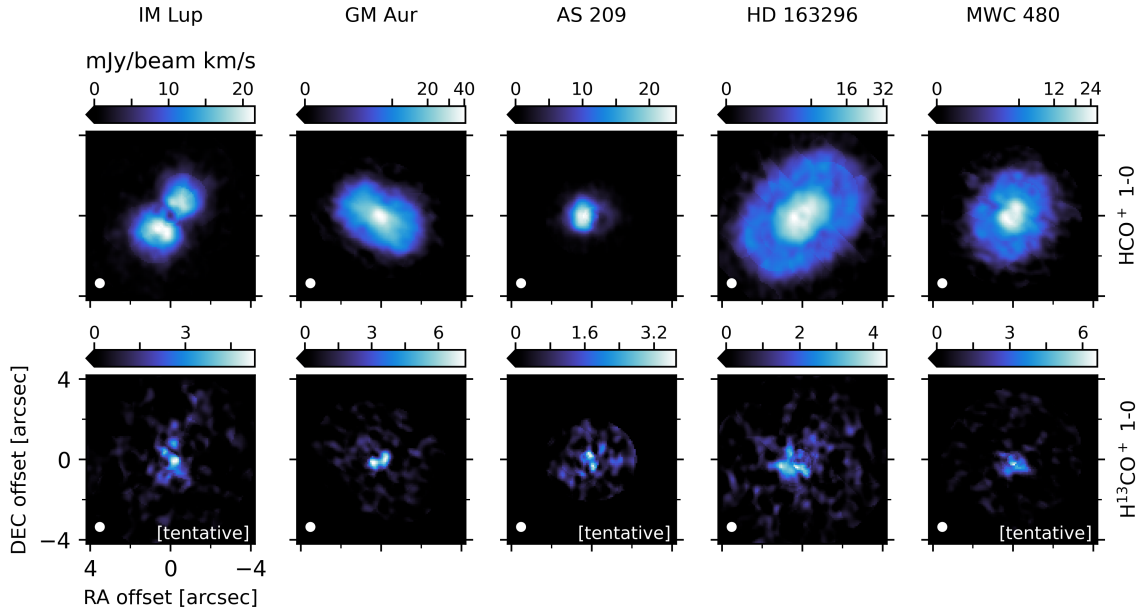


Figure 13. Same as figure 2, but for images tapered to a circular $0.5''$ beam.

Figure 14 shows the matched filter responses with the maximum SNR, while the radial extent of the corresponding Keplerian disk models is shown in the figure and also listed in Table 2. We note that the radial extent of the keplerian disk model roughly represents the radial extent of the emission. $\text{H}^{13}\text{CO}^+ J = 1 - 0$ is detected with a SNR above 6σ for GM Aur and HD 163296. The line is tentatively detected with a SNR above 3σ for IM Lup, AS 209 and MWC 480.

In Figure 15 we show the shifted and azimuthally averaged, disk-integrated $\text{H}^{13}\text{CO}^+ J = 1 - 0$ spectrum of each disk. The radial extent of the region over which we averaged is the same as for the matched filter. The disk-integrated spectra also point towards a detection in GM Aur and HD 163296, although at lower significance than the matched filter. In summary, we detect $\text{H}^{13}\text{CO}^+ J = 1 - 0$ towards GM Aur and IM Lup, and tentatively detect it towards the other three disks.

C. AZIMUTHALLY AVERAGED SPECTRA

Figure 16 show the azimuthally averaged spectra of HCO^+ and $\text{H}^{13}\text{CO}^+ J = 1 - 0$ together with model spectra from the MCMC fits.

D. DEPENDENCE OF HCO^+ COLUMN DENSITY ON ASSUMED EXCITATION TEMPERATURE

In our fiducial fits, the excitation temperature is a free parameter. In order to explore the dependence of our results on the excitation temperature, we performed additional fits where the excitation temperature is fixed to 30 K. Figure 17 displays a comparison of the column density profiles derived from the different fits. The comparison is discussed in Section 3.2. Figure 18 shows the optical depth profiles derived assuming $T_{\text{ex}} = 30$ K.

E. TEMPLATE DISK CHEMISTRY MODELS

To top panels in Figure 19 show the 2D (R, Z) distributions of the number of hydrogen nuclei and gas temperature in the template disk model. The panels in the second row show the abundances of gaseous CO, HCO^+ , and electron relative to hydrogen nuclei in the fiducial model. The panels in the third and fourth row are for the high C/O model and the low ζ model.

Figure 20 shows the absolute abundances (i.e. number density) of HCO^+ (top row), N_2H^+ (the second row), N_2D^+ (the third row), H_3^+ and its deuterated isotopomers (the fourth row) in the fiducial model (left), the high C/O model (middle), and the low ζ model (right).

REFERENCES

- Aikawa, Y., Furuya, K., Hincelin, U., & Herbst, E. 2018, ApJ, 855, 119, doi: [10.3847/1538-4357/aaad6c](https://doi.org/10.3847/1538-4357/aaad6c)
- Aikawa, Y., Furuya, K., Nomura, H., & Qi, C. 2015, ApJ, 807, 120, doi: [10.1088/0004-637X/807/2/120](https://doi.org/10.1088/0004-637X/807/2/120)

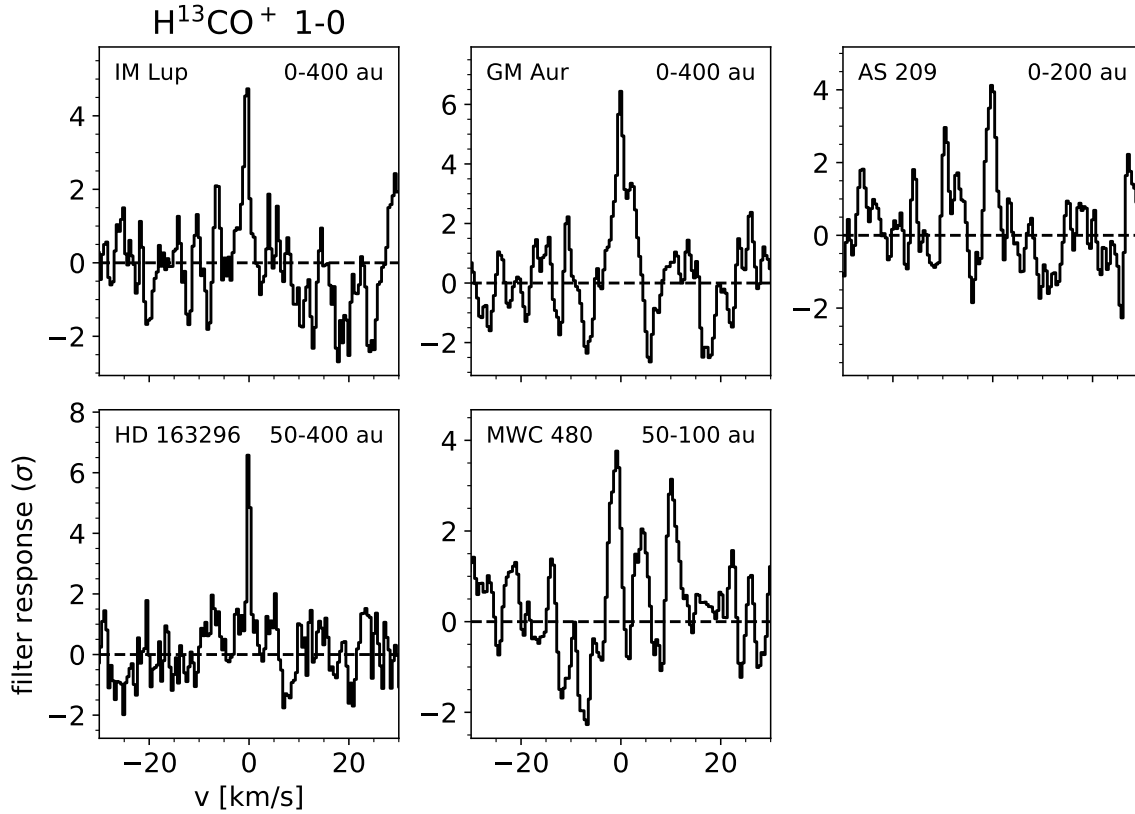


Figure 14. Matched filter response for H^{13}CO^+ $J = 1 - 0$. For each disk, we chose the Keplerian mask with the radius that maximized the SNR. The radial extent of that model is indicated in the upper right of each panel. The y-axis is in units of the noise in the filter response.

Aikawa, Y., & Herbst, E. 2001, *A&A*, 371, 1107,
doi: [10.1051/0004-6361:20010416](https://doi.org/10.1051/0004-6361:20010416)

Aikawa, Y., Miyama, S. M., Nakano, T., & Umebayashi, T. 1996, *ApJ*, 467, 684, doi: [10.1086/177644](https://doi.org/10.1086/177644)

Aikawa, Y., & Nomura, H. 2006, *ApJ*, 642, 1152,
doi: [10.1086/501114](https://doi.org/10.1086/501114)

Alarcón, F., & MAPS team. 2021, *ApJS*, 0, 0, doi: 0

Andrews, S. M., Huang, J., Pérez, L. M., et al. 2018, *ApJL*, 869, L41, doi: [10.3847/2041-8213/aaf741](https://doi.org/10.3847/2041-8213/aaf741)

Astropy Collaboration, Robitaille, T. P., Tollerud, E. J., et al. 2013, *A&A*, 558, A33,
doi: [10.1051/0004-6361/201322068](https://doi.org/10.1051/0004-6361/201322068)

Bai, X.-N., & Stone, J. M. 2013, *ApJ*, 769, 76,
doi: [10.1088/0004-637X/769/1/76](https://doi.org/10.1088/0004-637X/769/1/76)

Bergin, E. A., Aikawa, Y., Blake, G. A., & van Dishoeck, E. F. 2007, in *Protostars and Planets V*, ed. B. Reipurth, D. Jewitt, & K. Keil, 751.
<https://arxiv.org/abs/astro-ph/0603358>

Bergin, E. A., Cleeves, L. I., Crockett, N., & Blake, G. A. 2014, *Faraday Discussions*, 168, 61,
doi: [10.1039/C4FD00003J](https://doi.org/10.1039/C4FD00003J)

Bergin, E. A., Du, F., Cleeves, L. I., et al. 2016, *ApJ*, 831, 101, doi: [10.3847/0004-637X/831/1/101](https://doi.org/10.3847/0004-637X/831/1/101)

Béthune, W., Lesur, G., & Ferreira, J. 2017, *A&A*, 600, A75, doi: [10.1051/0004-6361/201630056](https://doi.org/10.1051/0004-6361/201630056)

Bosman, A. D., & MAPS team. 2021, *ApJS*, 0, 0, doi: 0

Bosman, A. D., Walsh, C., & van Dishoeck, E. F. 2018, *A&A*, 618, A182, doi: [10.1051/0004-6361/201833497](https://doi.org/10.1051/0004-6361/201833497)

Caselli, P., Walmsley, C. M., Zucconi, A., et al. 2002, *ApJ*, 565, 344, doi: [10.1086/324302](https://doi.org/10.1086/324302)

Cataldi, G., & MAPS team. 2021, *ApJS*, 0, 0, doi: 0

Chapillon, E., Parise, B., Guilloteau, S., & Du, F. 2011, *A&A*, 533, A143, doi: [10.1051/0004-6361/201117354](https://doi.org/10.1051/0004-6361/201117354)

Cieza, L. A., González-Ruilova, C., Hales, A. S., et al. 2021, *MNRAS*, 501, 2934, doi: [10.1093/mnras/staa3787](https://doi.org/10.1093/mnras/staa3787)

Cleeves, L. I., Bergin, E. A., & Adams, F. C. 2014, *ApJ*, 794, 123, doi: [10.1088/0004-637X/794/2/123](https://doi.org/10.1088/0004-637X/794/2/123)

Cleeves, L. I., Bergin, E. A., Qi, C., Adams, F. C., & Öberg, K. I. 2015, *ApJ*, 799, 204,
doi: [10.1088/0004-637X/799/2/204](https://doi.org/10.1088/0004-637X/799/2/204)

Czekala, I., & MAPS team. 2021, *ApJS*, 0, 0, doi: 0

Dalgarno, A. 2006, *Proceedings of the National Academy of Science*, 103, 12269, doi: [10.1073/pnas.0602117103](https://doi.org/10.1073/pnas.0602117103)

Dionatos, O., Woitke, P., Güdel, M., et al. 2019, *A&A*, 625, A66, doi: [10.1051/0004-6361/201832860](https://doi.org/10.1051/0004-6361/201832860)

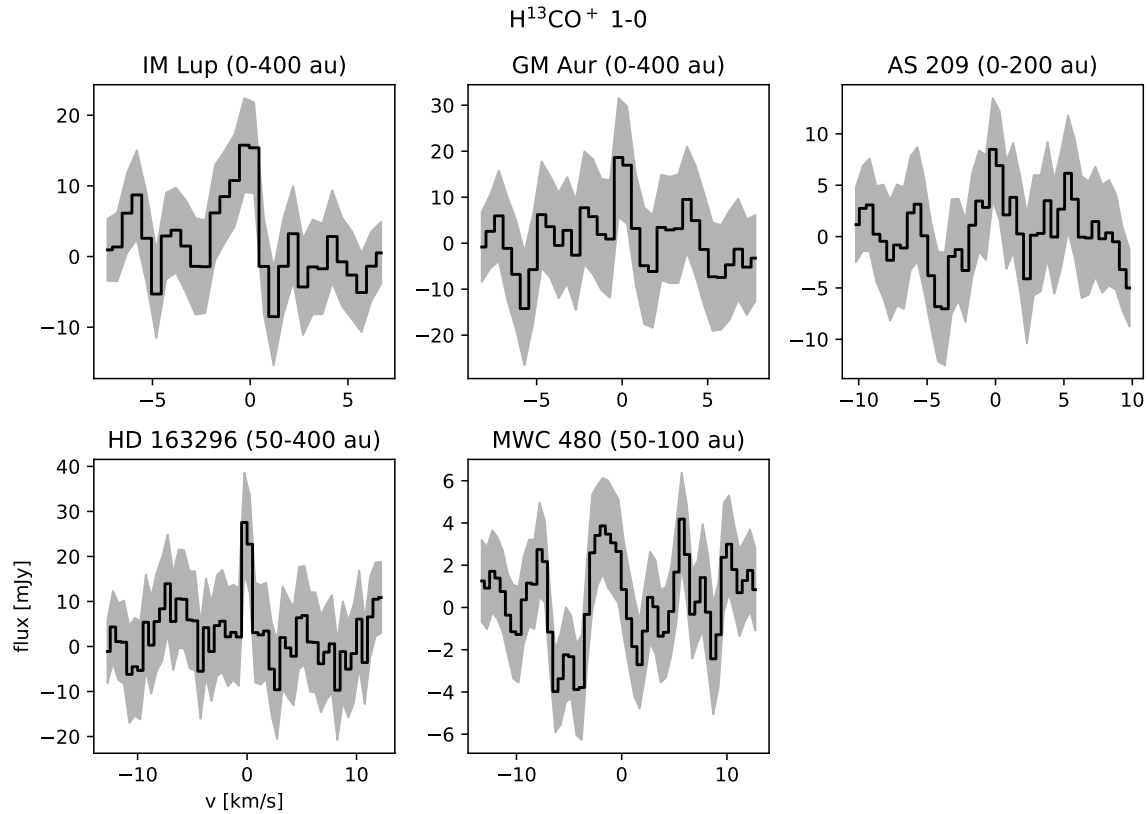


Figure 15. Disk-integrated spectra (over the radial range indicated in the title of each panel) of $\text{H}^{13}\text{CO}^+ J = 1 - 0$. The spectrum at each spatial location of the data cube was shifted to the systemic velocity prior to integration. The shaded region corresponds to the 1σ error.

- Duley, W. W., & Williams, Williams, A. 1984, *Interstellar Chemistry* (Academic Press)
- Endres, C. P., Schlemmer, S., Schilke, P., Stutzki, J., & Müller, H. S. P. 2016, *Journal of Molecular Spectroscopy*, 327, 95, doi: [10.1016/j.jms.2016.03.005](https://doi.org/10.1016/j.jms.2016.03.005)
- Favre, C., Fedele, D., Maud, L., et al. 2019, *ApJ*, 871, 107, doi: [10.3847/1538-4357/aaf80c](https://doi.org/10.3847/1538-4357/aaf80c)
- Fedele, D., Tazzari, M., Booth, R., et al. 2018, *A&A*, 610, A24, doi: [10.1051/0004-6361/201731978](https://doi.org/10.1051/0004-6361/201731978)
- Flaherty, K. M., Hughes, A. M., Rose, S. C., et al. 2017, *ApJ*, 843, 150, doi: [10.3847/1538-4357/aa79f9](https://doi.org/10.3847/1538-4357/aa79f9)
- Foreman-Mackey, D., Hogg, D. W., Lang, D., & Goodman, J. 2013, *PASP*, 125, 306, doi: [10.1086/670067](https://doi.org/10.1086/670067)
- Fujimoto, Y., Krumholz, M. R., & Tachibana, S. 2018, *MNRAS*, 480, 4025, doi: [10.1093/mnras/sty2132](https://doi.org/10.1093/mnras/sty2132)
- Furuya, K., & Aikawa, Y. 2014, *ApJ*, 790, 97, doi: [10.1088/0004-637X/790/2/97](https://doi.org/10.1088/0004-637X/790/2/97)
- Glassgold, A. E., Najita, J., & Igea, J. 1997, *ApJ*, 480, 344, doi: [10.1086/303952](https://doi.org/10.1086/303952)
- Huang, J., Andrews, S. M., Dullemond, C. P., et al. 2018, *ApJL*, 869, L42, doi: [10.3847/2041-8213/aaf740](https://doi.org/10.3847/2041-8213/aaf740)
- Hunter, J. D. 2007, *Computing in Science & Engineering*, 9, 90, doi: [10.1109/MCSE.2007.55](https://doi.org/10.1109/MCSE.2007.55)
- Jonkheid, B., Dullemond, C. P., Hogerheijde, M. R., & van Dishoeck, E. F. 2007, *A&A*, 463, 203, doi: [10.1051/0004-6361:20065668](https://doi.org/10.1051/0004-6361:20065668)
- Kama, M., Bruderer, S., van Dishoeck, E. F., et al. 2016, *A&A*, 592, A83, doi: [10.1051/0004-6361/201526991](https://doi.org/10.1051/0004-6361/201526991)
- Krijt, S., Schwarz, K. R., Bergin, E. A., & Ciesla, F. J. 2018, *ApJ*, 864, 78, doi: [10.3847/1538-4357/aad69b](https://doi.org/10.3847/1538-4357/aad69b)
- Law, C., & MAPS team. 2021a, *ApJS*, 0, 0, doi: 0
- . 2021b, *ApJS*, 0, 0, doi: 0
- Liu, Y., Dipierro, G., Ragusa, E., et al. 2019, *A&A*, 622, A75, doi: [10.1051/0004-6361/201834157](https://doi.org/10.1051/0004-6361/201834157)
- Long, F., Pinilla, P., Herczeg, G. J., et al. 2018, *ApJ*, 869, 17, doi: [10.3847/1538-4357/aae8e1](https://doi.org/10.3847/1538-4357/aae8e1)
- Loomis, R. A., Öberg, K. I., Andrews, S. M., et al. 2018, *AJ*, 155, 182, doi: [10.3847/1538-3881/aab604](https://doi.org/10.3847/1538-3881/aab604)
- Matrà, L., MacGregor, M. A., Kalas, P., et al. 2017, *ApJ*, 842, 9, doi: [10.3847/1538-4357/aa71b4](https://doi.org/10.3847/1538-4357/aa71b4)
- McMullin, J. P., Waters, B., Schiebel, D., Young, W., & Golap, K. 2007, in *Astronomical Society of the Pacific Conference Series*, Vol. 376, *Astronomical Data Analysis Software and Systems XVI*, ed. R. A. Shaw, F. Hill, & D. J. Bell, 127

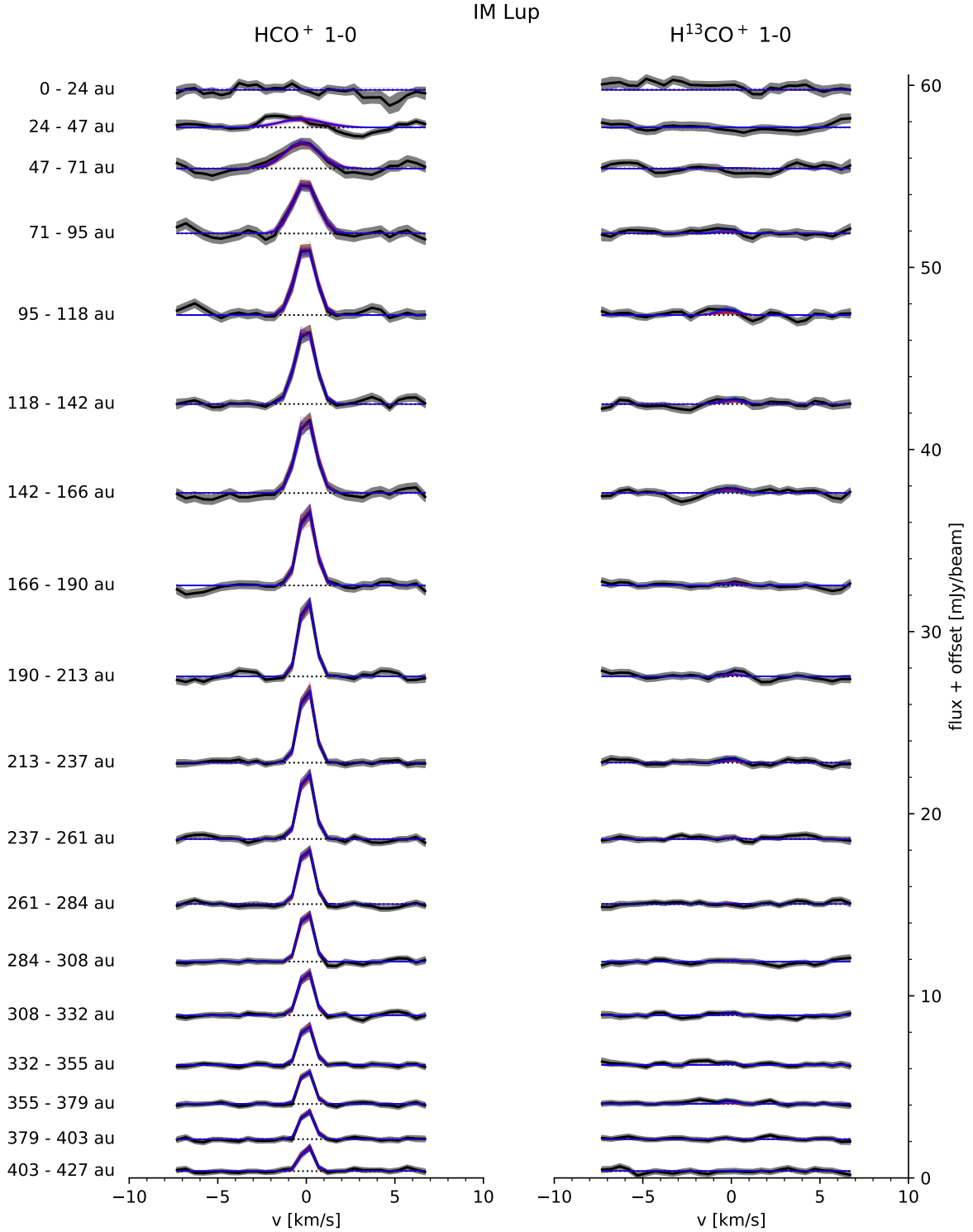


Figure 16a. The black curves show azimuthally averaged spectra for IM Lup. Spectra are vertically offset for clarity. The shaded region marks the 1σ error. The horizontal dotted line marks the zero flux level. For each spectrum, we show 20 randomly selected model spectra from the MCMC with the blue curves (T_{ex} as free parameter) and the red curves (T_{ex} fixed to 30 K). The selection probability of each model was set proportional to its posterior probability. Most of the time, the model spectra overlap closely, so that only the blue curves are visible.

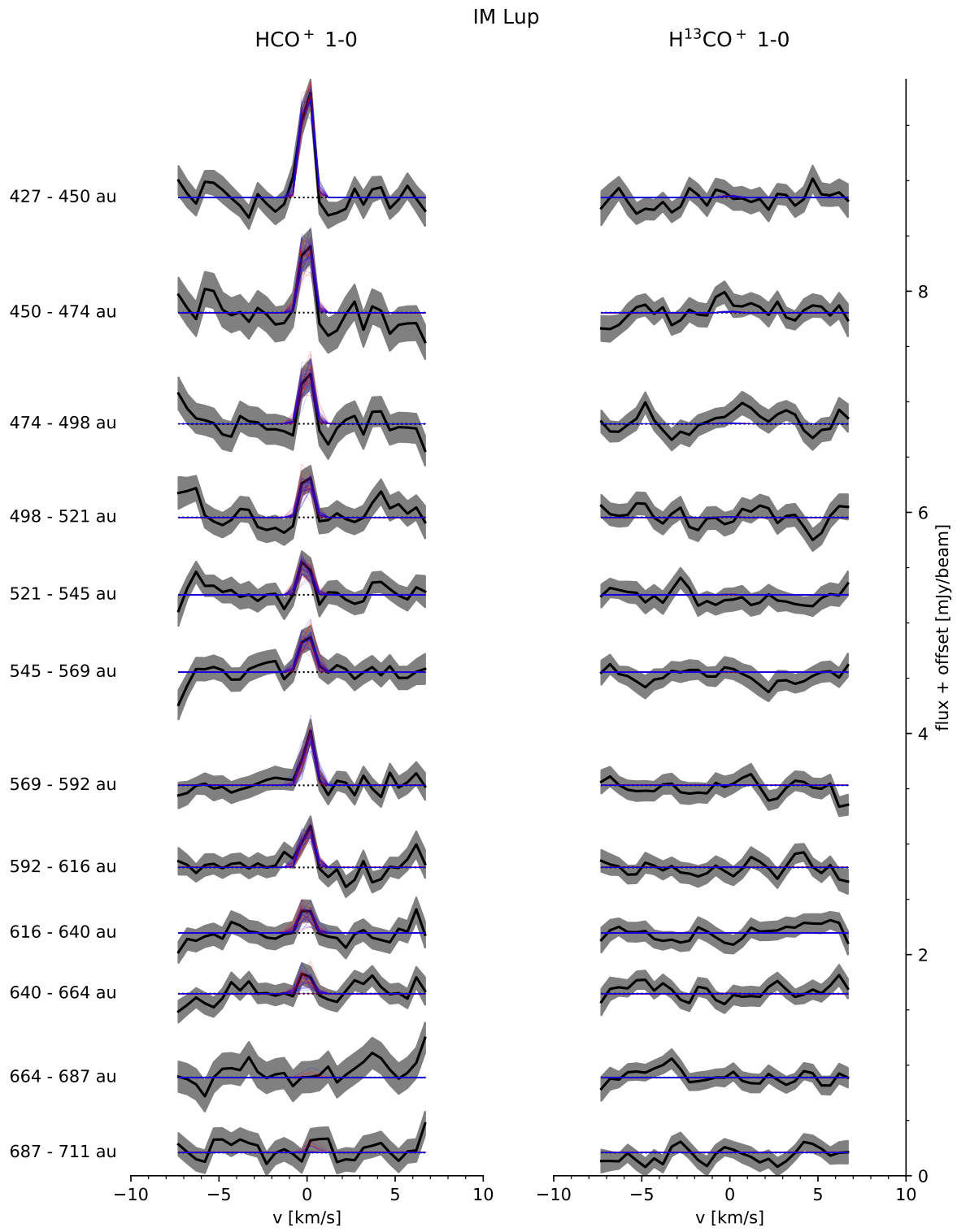


Figure 16b. Continuation of figure 16a.

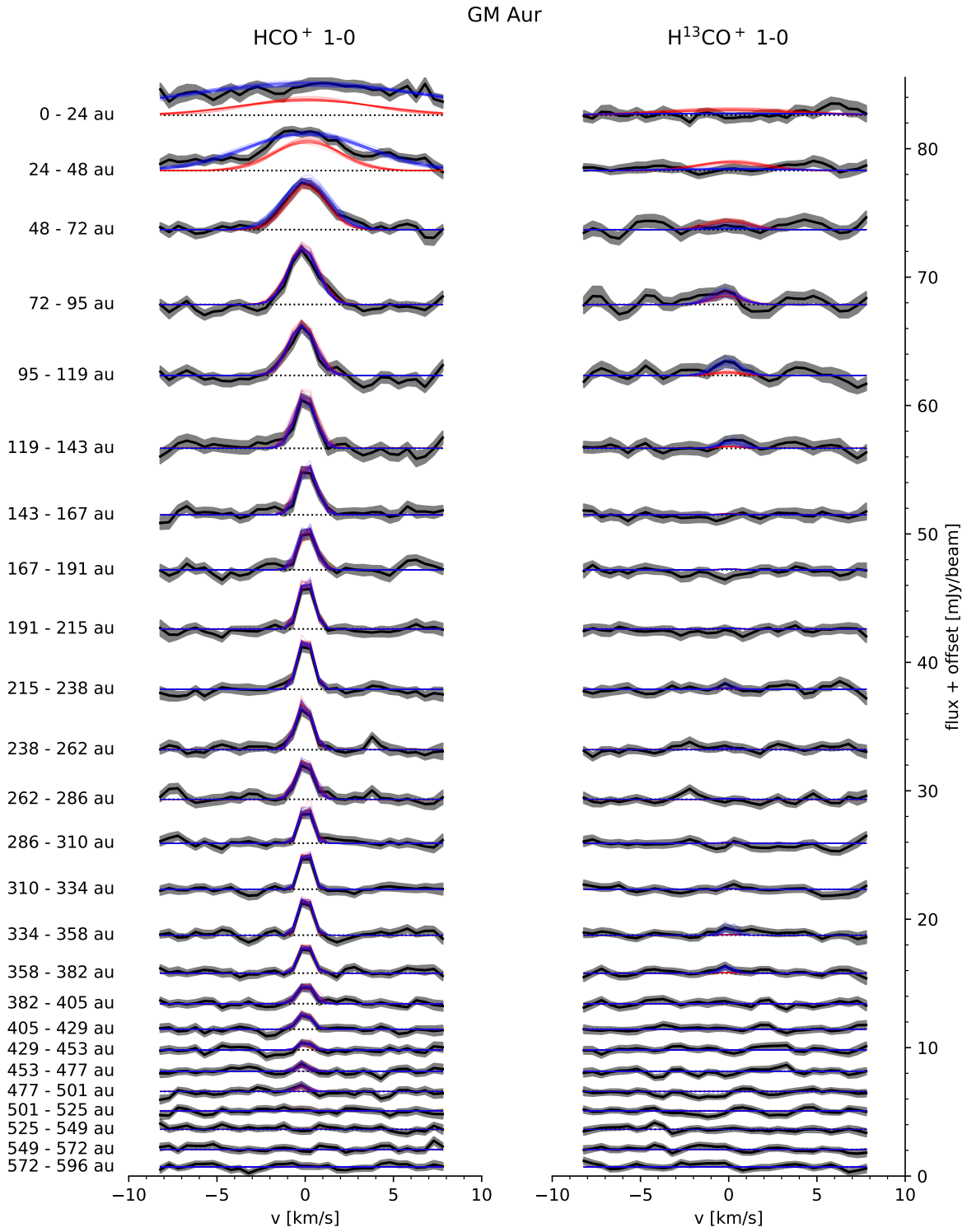


Figure 16c. Same as figure 16a, but for GM Aur.

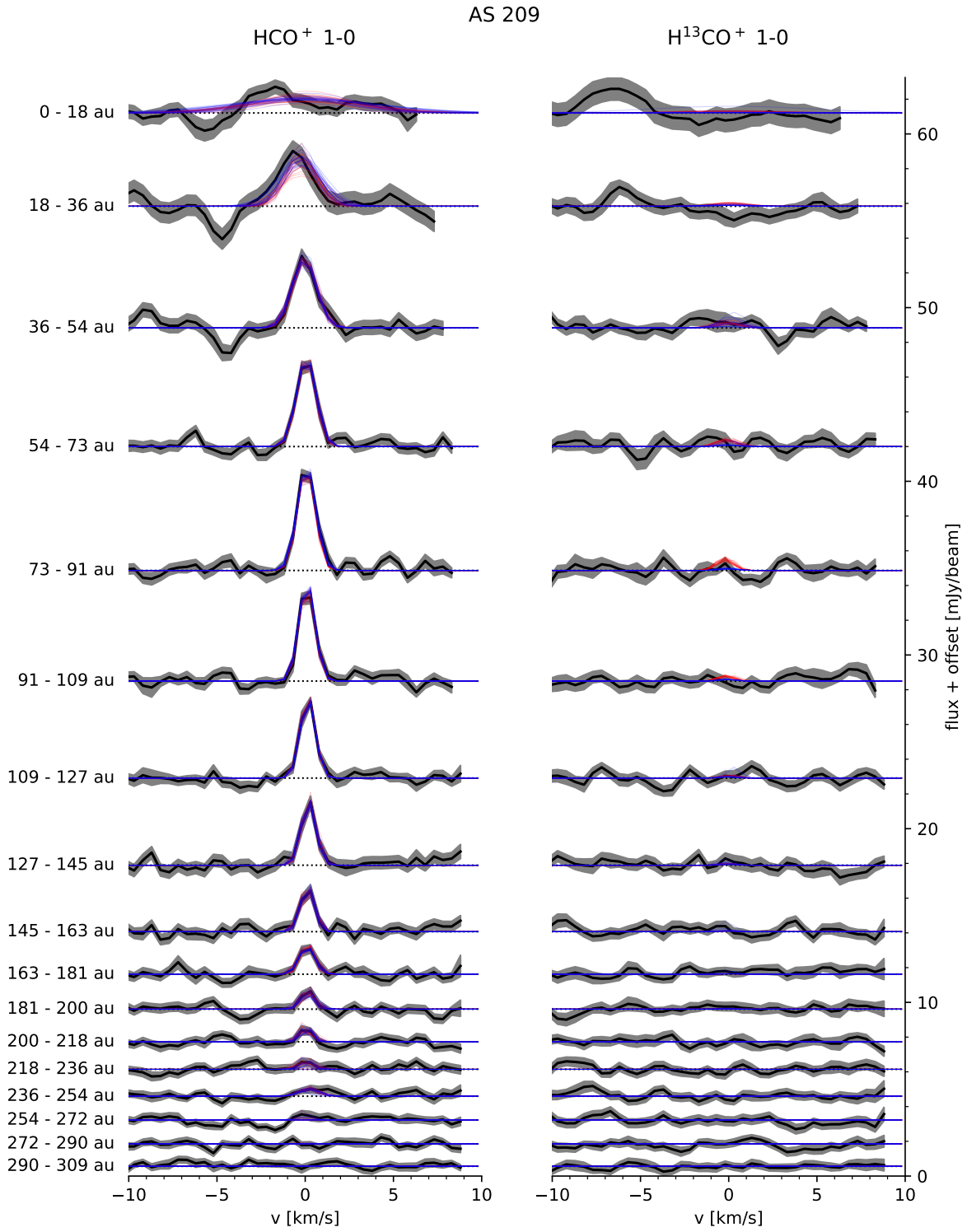


Figure 16d. Same as figure 16a, but for AS 209.

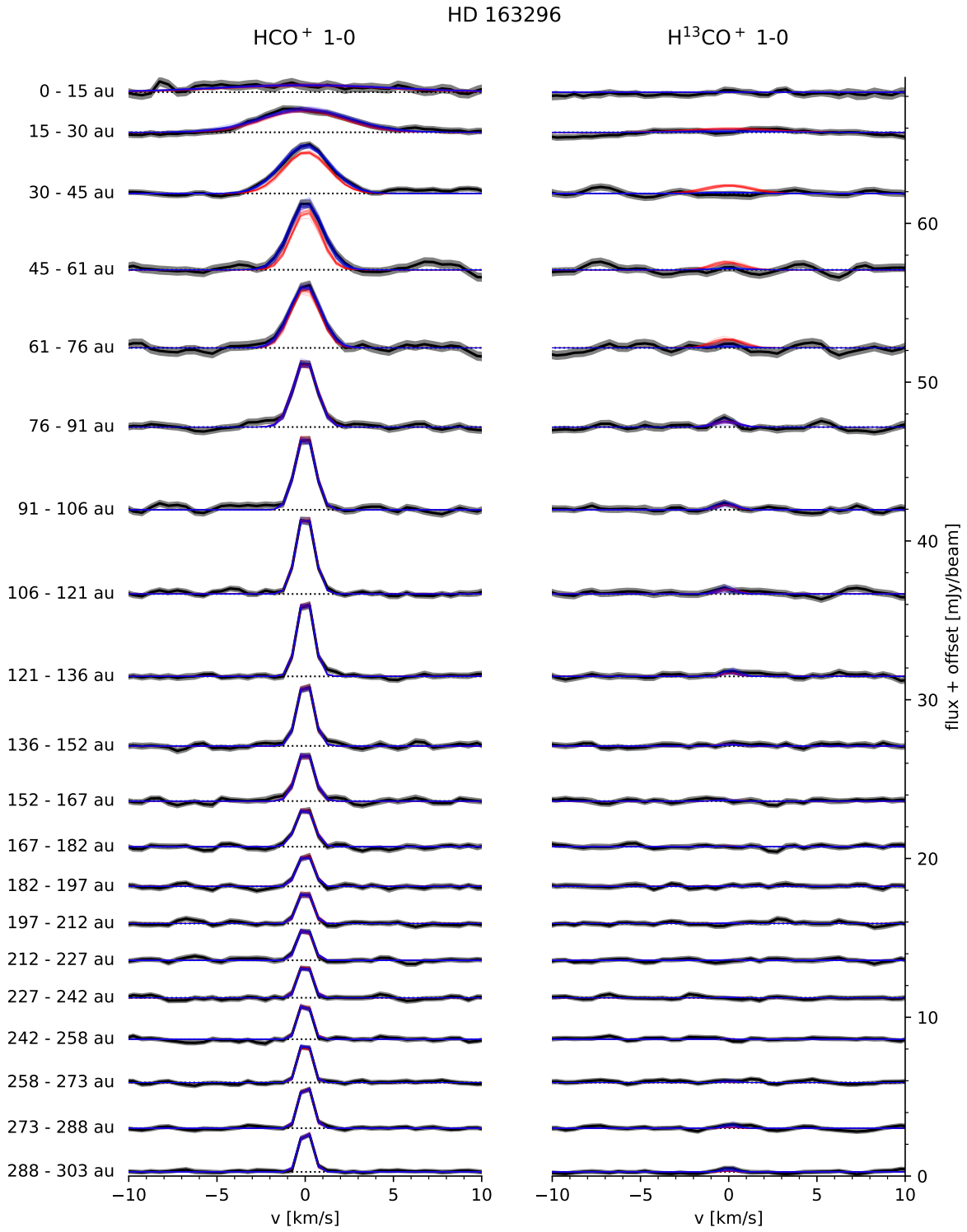


Figure 16e. Same as figure 16a, but for HD 163296.

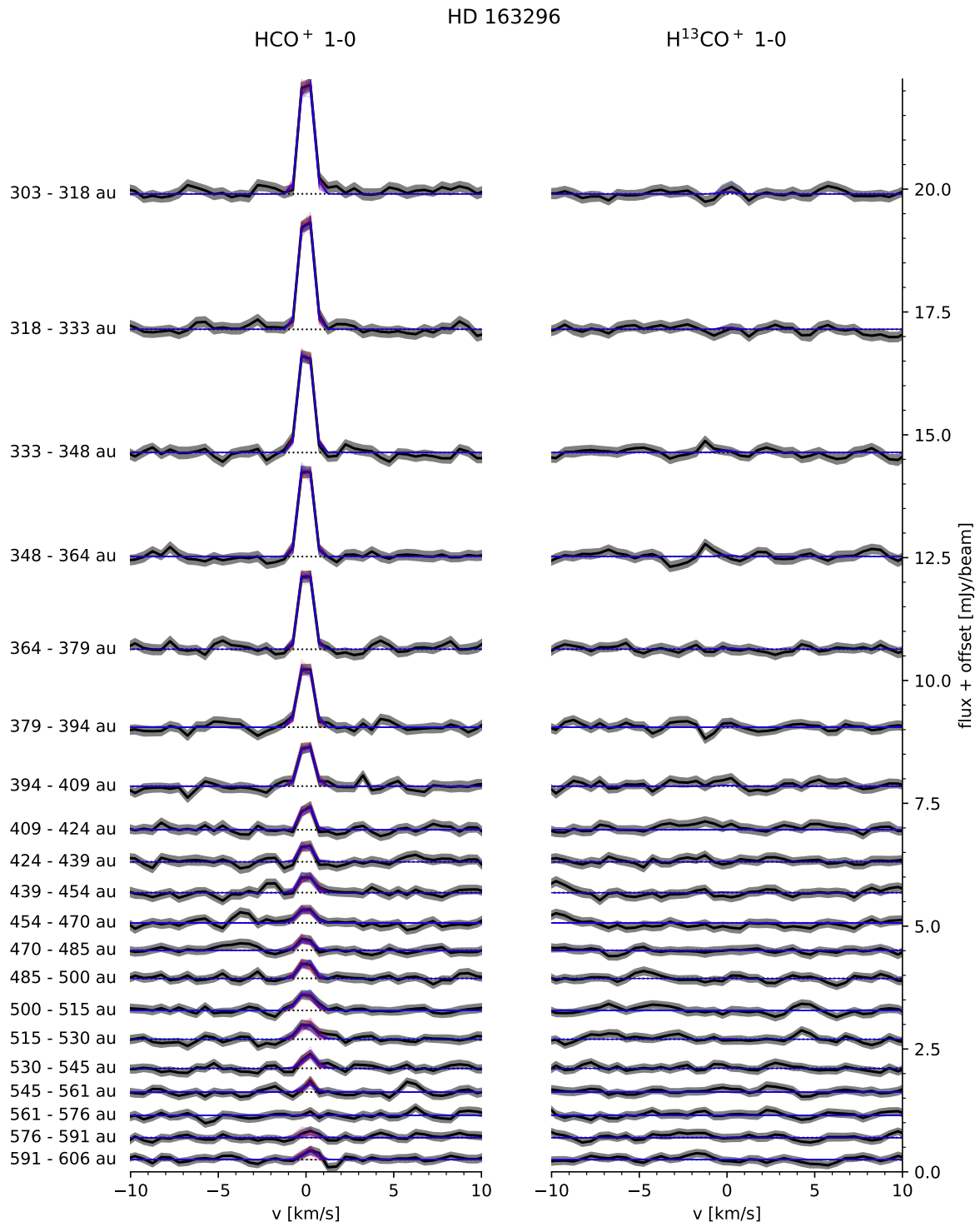


Figure 16f. Continuation of figure 16e.

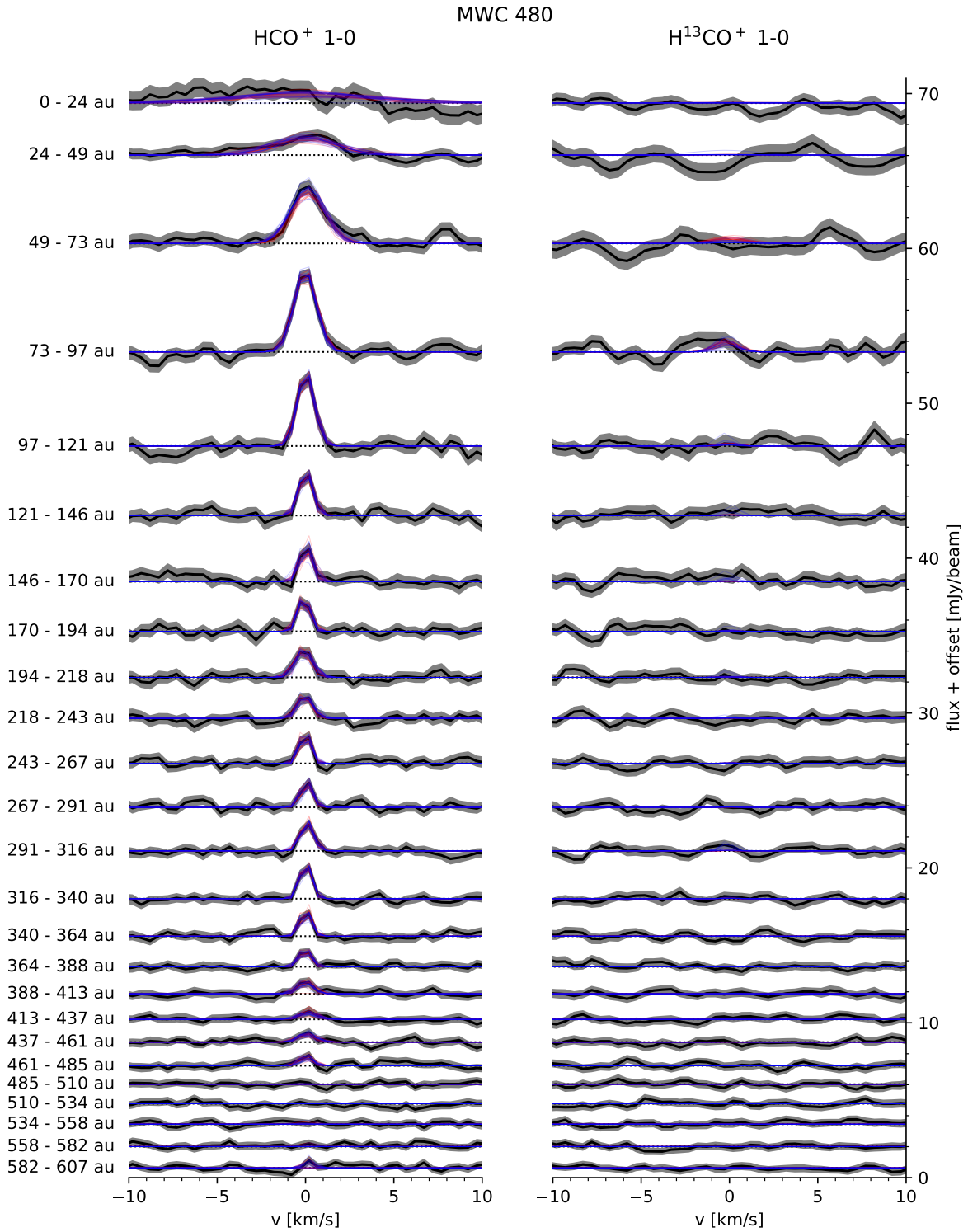


Figure 16g. Same as figure 16a, but for MWC 480.

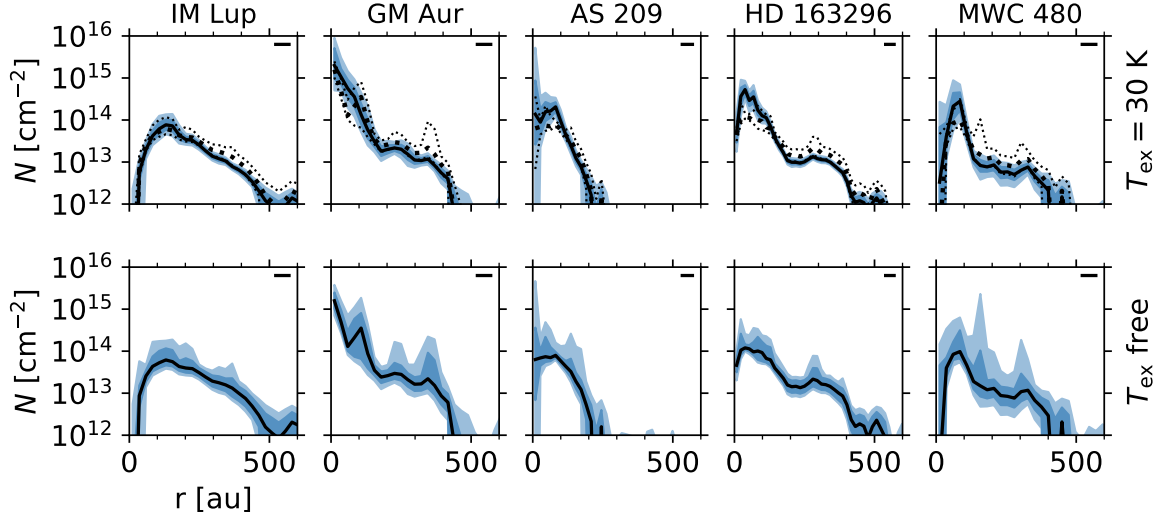


Figure 17. The column density of HCO^+ assuming an excitation temperature of 30 K (top row) and for our fiducial fits where T_{ex} is a free parameter (bottom row). The black solid lines mark the median, while the shading encompasses the regions from the 16th to 84th and the 2.3th to 97.7th percentile, respectively. To ease comparison, in the top panel, the thick and thin black dotted lines mark the median and the 16th and 84th percentile of the fits where T_{ex} is a free parameter.

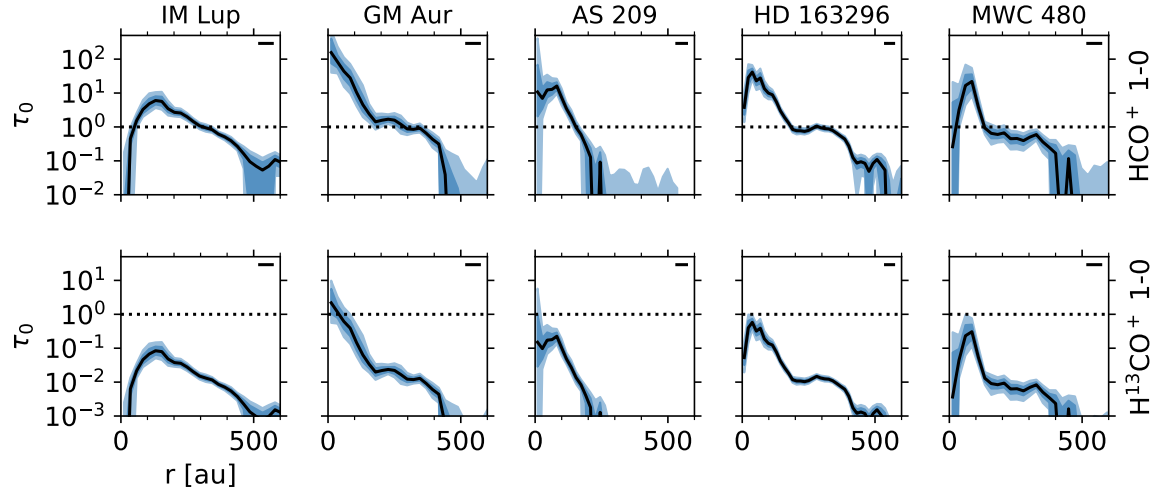


Figure 18. Optical depth profiles of HCO^+ ($J = 1 - 0$) and H^{13}CO^+ ($J = 1 - 0$) derived from fitting azimuthally averaged spectra assuming $T_{\text{ex}} = 30$ K. The black lines mark the median, while the shading encompasses the regions from the 16th to 84th and the 2.3th to 97.7th percentile, respectively.

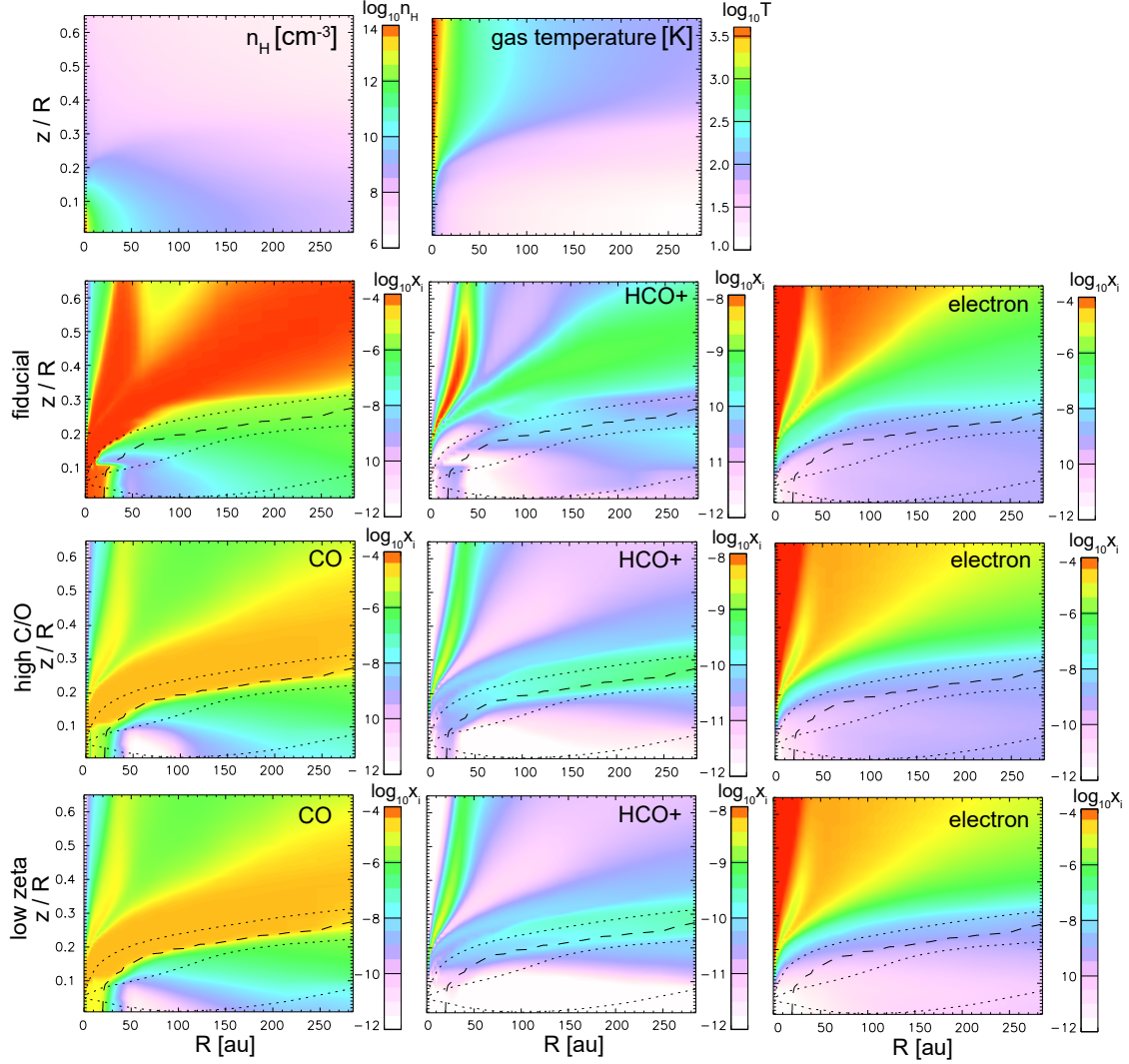


Figure 19. Number density of hydrogen nuclei (n_{H}) and gas temperature of the template disk model are shown in the top row. Furthermore, we show the abundances of CO (left column), HCO^+ (middle column), and electrons (right column) relative to hydrogen nuclei in the fiducial model (second row), CO depleted model (third row), and the model without CR ionization (low ζ model, bottom row).

Milam, S. N., Savage, C., Brewster, M. A., Ziurys, L. M., & Wyckoff, S. 2005, *ApJ*, 634, 1126, doi: [10.1086/497123](https://doi.org/10.1086/497123)

Müller, H. S. P., Thorwirth, S., Roth, D. A., & Winnewisser, G. 2001, *A&A*, 370, L49, doi: [10.1051/0004-6361:20010367](https://doi.org/10.1051/0004-6361:20010367)

Öberg, K. I., & MAPS team. 2021, *ApJS*, 0, 0, doi: 0

Öberg, K. I., Qi, C., Wilner, D. J., & Andrews, S. M. 2011a, *ApJ*, 743, 152, doi: [10.1088/0004-637X/743/2/152](https://doi.org/10.1088/0004-637X/743/2/152)

Öberg, K. I., Qi, C., Fogel, J. K. J., et al. 2011b, *ApJ*, 734, 98, doi: [10.1088/0004-637X/734/2/98](https://doi.org/10.1088/0004-637X/734/2/98)

Padovani, M., Ivlev, A. V., Galli, D., & Caselli, P. 2018, *A&A*, 614, A111, doi: [10.1051/0004-6361/201732202](https://doi.org/10.1051/0004-6361/201732202)

Price-Whelan, A. M., Sipőcz, B. M., Günther, H. M., et al. 2018, *AJ*, 156, 123, doi: [10.3847/1538-3881/aabc4f](https://doi.org/10.3847/1538-3881/aabc4f)

Qi, C., Öberg, K. I., & Wilner, D. J. 2013a, *ApJ*, 765, 34, doi: [10.1088/0004-637X/765/1/34](https://doi.org/10.1088/0004-637X/765/1/34)

Qi, C., Öberg, K. I., Wilner, D. J., et al. 2013b, *Science*, 341, 630, doi: [10.1126/science.1239560](https://doi.org/10.1126/science.1239560)

Qi, C., Öberg, K. I., Espaillat, C. C., et al. 2019, *ApJ*, 882, 160, doi: [10.3847/1538-4357/ab35d3](https://doi.org/10.3847/1538-4357/ab35d3)

Rab, C., Güdel, M., Padovani, M., et al. 2017, *A&A*, 603, A96, doi: [10.1051/0004-6361/201630241](https://doi.org/10.1051/0004-6361/201630241)

Rab, C., Güdel, M., Woitke, P., et al. 2018, *A&A*, 609, A91, doi: [10.1051/0004-6361/201731443](https://doi.org/10.1051/0004-6361/201731443)

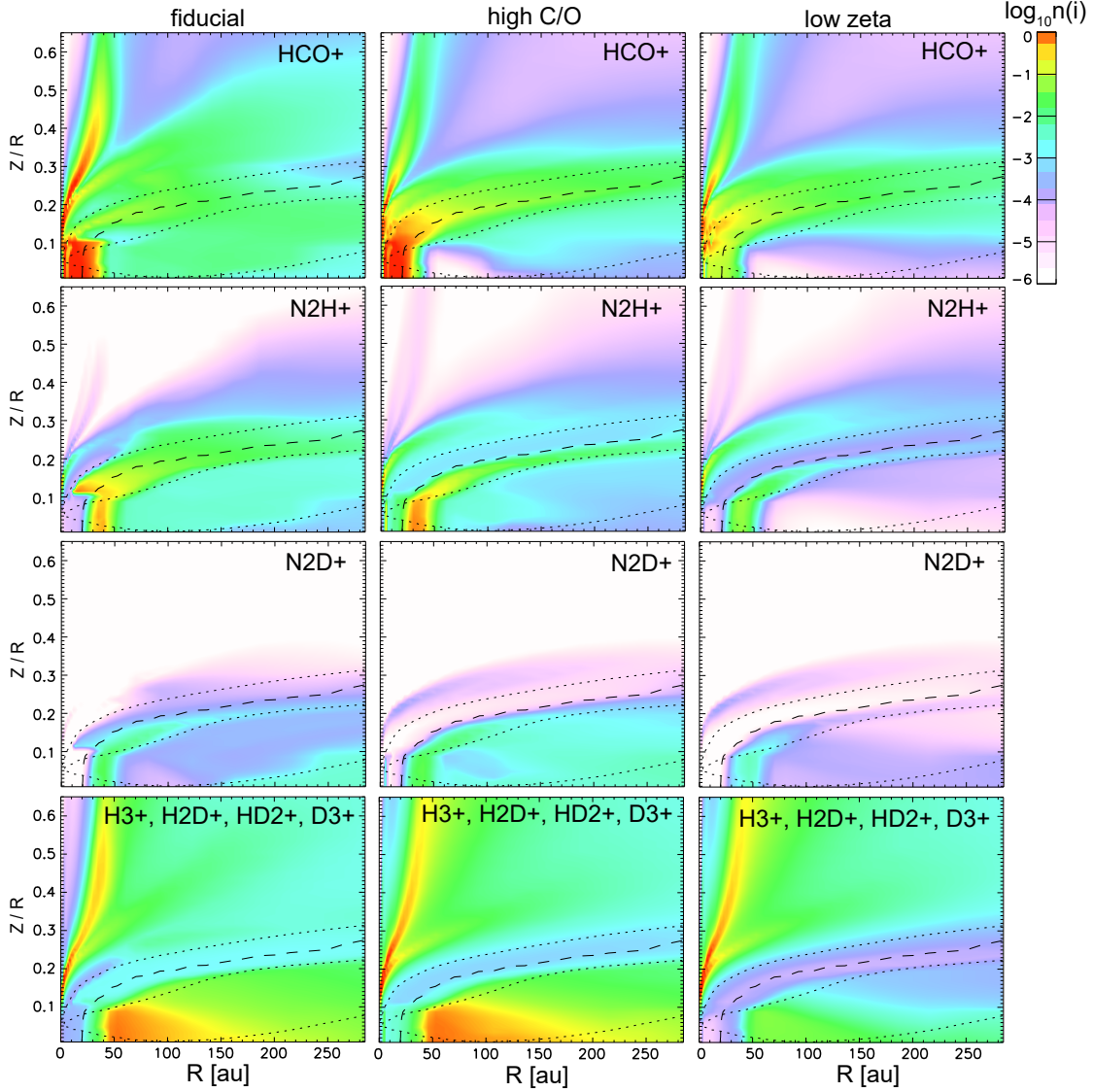


Figure 20. Absolute abundance (i.e. number density in units of cm^{-3}) of major molecular ions in the fiducial disk model (left column), high C/O model (middle column), and low ζ model (right column).

Schwarz, K. R., Bergin, E. A., Cleaves, L. I., et al. 2018,

ApJ, 856, 85, doi: [10.3847/1538-4357/aaae08](https://doi.org/10.3847/1538-4357/aaae08)

Sierra, A., & MAPS team. 2021, ApJS, 0, 0, doi: 0

Smirnov-Pinchukov, G. V., Semenov, D. A., Akimkin,

V. V., & Henning, T. 2020, A&A, 644, A4,

doi: [10.1051/0004-6361/202038572](https://doi.org/10.1051/0004-6361/202038572)

Suzuki, T. K., & Inutsuka, S.-i. 2009, ApJL, 691, L49,

doi: [10.1088/0004-637X/691/1/L49](https://doi.org/10.1088/0004-637X/691/1/L49)

Teague, R. 2019, The Journal of Open Source Software, 4,

1632, doi: [10.21105/joss.01632](https://doi.org/10.21105/joss.01632)

Teague, R., Bae, J., Bergin, E. A., Birnstiel, T., &

Foreman-Mackey, D. 2018a, ApJL, 860, L12,

doi: [10.3847/2041-8213/aac6d7](https://doi.org/10.3847/2041-8213/aac6d7)

Teague, R., Bae, J., Birnstiel, T., & Bergin, E. A. 2018b,

ApJ, 868, 113, doi: [10.3847/1538-4357/aae836](https://doi.org/10.3847/1538-4357/aae836)

Teague, R., & Foreman-Mackey, D. 2018, Research Notes of

the American Astronomical Society, 2, 173,

doi: [10.3847/2515-5172/aae265](https://doi.org/10.3847/2515-5172/aae265)

Teague, R., Semenov, D., Guilloteau, S., et al. 2015, A&A,

574, A137, doi: [10.1051/0004-6361/201425268](https://doi.org/10.1051/0004-6361/201425268)

Teague, R., Guilloteau, S., Semenov, D., et al. 2016, A&A,

592, A49, doi: [10.1051/0004-6361/201628550](https://doi.org/10.1051/0004-6361/201628550)

Umeyayashi, T., & Nakano, T. 1981, PASJ, 33, 617

—. 1988, Progress of Theoretical Physics Supplement, 96,

151, doi: [10.1143/PTPS.96.151](https://doi.org/10.1143/PTPS.96.151)

—. 2009, ApJ, 690, 69, doi: [10.1088/0004-637X/690/1/69](https://doi.org/10.1088/0004-637X/690/1/69)

- van der Walt, S., Colbert, S. C., & Varoquaux, G. 2011, *Computing in Science and Engineering*, 13, 22, doi: [10.1109/MCSE.2011.37](https://doi.org/10.1109/MCSE.2011.37)
- Virtanen, P., Gommers, R., Oliphant, T. E., et al. 2020, *Nature Methods*, doi: <https://doi.org/10.1038/s41592-019-0686-2>
- Wakelam, V., Chapillon, E., Dutrey, A., et al. 2019, *MNRAS*, 484, 1563, doi: [10.1093/mnras/stz068](https://doi.org/10.1093/mnras/stz068)
- Willacy, K. 2007, *ApJ*, 660, 441, doi: [10.1086/512796](https://doi.org/10.1086/512796)
- Wilson, T. L. 1999, *Reports on Progress in Physics*, 62, 143, doi: [10.1088/0034-4885/62/2/002](https://doi.org/10.1088/0034-4885/62/2/002)
- Yen, H.-W., Koch, P. M., Liu, H. B., et al. 2016, *ApJ*, 832, 204, doi: [10.3847/0004-637X/832/2/204](https://doi.org/10.3847/0004-637X/832/2/204)
- Zhang, K., & MAPS team. 2021, *ApJS*, 0, 0, doi: 0